**ROCKWELL
SCIENTIFIC**

# High Temperature Coatings by Pulsed Electron Beam Ablation

Final Report

Contract Number N00014-02-C-0025

*prepared for*

Office of Naval Research
800 North Quincy St.
Arlington, VA 22217-5660
Dr. S. Fishman

*Prepared by*

Olivier Sudre
David B. Marshall
Sergio Lucato

Rockwell Scientific
1049 Camino Dos Rios
Thousand Oaks, CA 91360

August 2005

# Table of contents

# 1 Summary

The objective of this program was to investigate the deposition and properties of new high temperature coatings using pulsed-electron-beam ablation (PEBA) and to characterize the corrosion of those compounds in relevant environments.

The PEBA technique has potential advantages for depositing compounds that are known to be difficult to deposit by conventional electron-beam evaporation. The use of ablation rather than melting and evaporation avoids changes in composition associated with differing evaporation rates of constituents in a molten target. The use of electrons rather than eximer laser radiation (as in conventional laser ablation methods) enables ablation of materials that do not couple well to the laser because they are partly transparent at the laser wavelength or reflective. Using a chamber with stationary and rotating heated substrates, coatings of both lanthanum phosphate and lanthanum silicate were successfully deposited. Rare-earth phosphates are of interest for thermal barrier coatings, while rare-earth silicates are of interest for environmental barrier coatings.

The coatings deposited at high temperature were crystalline. However, when stoichiometric targets were used, the coating stoichiometry was always deficient in the lighter elements, phosphorous and silicon. A model experiment was designed to map out the stoichiometry of the gas phase as a function of distance from the center of the plume. The results showed that the non-stoichiometry was the result of a faster diffusion rate of the lighter elements away from the center of the plume, likely due to collisions with the heavier rare-earth element. In the case of $LaPO_4$, the loss of phosphorous could be compensated for by using a phosphorous-rich target, thus leading to deposition of stoichiometric monazite $LaPO_4$ as the major phase on the substrate. However, the limited size of the region of stoichiometry precludes the use of this technique for producing uniform coatings on large specimens in our current configuration. Furthermore, we found that the rate of deposition (~1μm/hour) was too slow for producing coatings of thicknesses required for thermal or environmental barrier coating technology.

We also developed an efficient laboratory-scale facility to assess the stability and degradation of thermal and environmental barrier coatings (TBCs and EBCs) in high temperature, high-velocity water-vapor conditions representative of full-scale gas turbine engine environments. The technique relies on the use of a high-speed, high-temperature vapor jet formed by feeding water at a controlled rate into a capillary tube inside a tube furnace (Fig. 2), where the large expansion of vaporization within the confines of the capillary accelerates the jet. Water vapor corrosion rates of ~1 μm/hour have been demonstrated on SiC for a range of temperature and velocity conditions. This new technique opens the way for economical characterization of candidate high-temperature materials and coatings for use in combustion components.

# 2 List of figures

*Figure 1: Pulsed electron beam source and power supply.*

*Figure 2: (A) Pulsed Electron Beam chamber, (B) Schematic indicating some of the main parameters (D is target to substrate distance, d is gun tip to target distance).*

*Figure 3: (A) Flash observed during the interaction of the beam pulse with the target, forming a plasma plume in front of the substrate holder (B) Coated FeCrAlY and glass substrates set on substrate holder.*

*Figure 4: Configuration of pulsed e-beam deposition with a rotating substrate at thigh temperature.*

*Figure 5: (A) Low magnification of the alumina coating on oxidized FeCrAlY (1Hz, 15 min.), (B) alumina islands deposited on the substrate.*

*Figure 6: Continuous alumina coating deposited on polished FeCrAlY substrate (3 Hz, 40 min.). The coating was spalled by scribing the surface using a sharp steel tool.*

*Figure 7: Y-ZrO2 coating formed by pulsed e-beam deposition on pre-oxidized FeCrAlY substrate: cracks normal to coating were formed by bending the coated substrate around a sharp radius.*

*Figure 8: (A) Lanthanum phosphate coating on an oxidized FeCrAlY substrate (~5 Hz, 30 min.), (B) cross-section view of the coating after spallation of the coating after scribing the surface.*

*Figure 9: (A) Lanthanum phosphate coating on an oxidized FeCrAlY substrate (~7 Hz, 60 min.), (B) cross-section view of the coating after spallation of the coating after scribing the surface.*

*Figure 10: X-ray diffraction of lanthanum phosphate coatings deposited by EBPVD and PED on low temperature substrates.*

*Figure 11. (a) La-phosphate coating formed by pulsed e-beam deposition on pre-oxidized FeCrAlY substrate. (b) X-ray diffraction data from coatings deposited on substrates heated to temperatures indicated.*

*Figure 12: Microstructures of $La_3PO_7$ deposited coatings on rotating substrate of $Al_2O_3$ with substrate temperatures of 670-980 °C (a and b) and 750-1070 °C (c and d)*

*Figure 13: X-ray diffraction patterns of coatings deposited from a porous target of $LaPO_4$.*

*Figure 14: La-silicate coatings deposited on substrates heated to (a) 863 °C and (b) 883 °C*

*Fig. 15. X-ray diffraction data from La-silicate coatings formed by pulsed e-beam deposition: (a) substrate heated to temperatures shown; (b) deposited on substrate at room temperature then heated to temperatures shown; and (c) deposited at 780 °C then heated to temperatures shown.*

*Figure 16. (a) Phase diagram for $La_2O_3 - SiO_2$ system [1]. (b) Formation enthalpy for various rare-earth silicates [2]*

*Figure 17: Configuration of witness foils placed on each side of the substrate.*

*Figure 18: (a) Location of measurement along the foil and on substrate, (b) analysis of peak height for P and La, (c) La/P ratio on substrate and along the foil length.*

*Figure 19: Phase diagram of $La_2O_3$-$P_2O_5$, indicating the composition of $La_3PO_7$, $LaPO_4$ and 50 $La_2O_3$-50 $P_2O_5$ respectively from left to right.*

*Figure 20: (a) Concentration profile of La and P along the foil, (b) La/P ratio along the foil and on the target.*

*Figure 21: (a) Microstructure of coating deposited from P-rich target. (b) X-diffraction patterns showing the presence of $LaPO_4$, $La_3PO_7$ and $La_2P_4O_{13}$.*

*Figure 22: Monazite surface after spalling of the layer of $Na_2SO_4$ salt molten at 900 °C(Tm+16 °C)*

*Figure 23: Reaction of monazite with $NaVO_3$ salt at 650 °C (Tm+20 °C) (a) view of drilled hole with molten salt inside (b) and (c) details of the framed regions in (a) and (b) respectively showing the partial dissolution of the monazite grains into the salt.*

*Fig. 24. (a) Schematic of water jet test set-up. (b) Photograph showing support fixture and wedge-shaped SiC test specimen in front of the capillary tube.*

*Fig. 25. Maps of steady-state conditions in terms of gas velocity and total pressure for hydrocarbon combustion at 1316 °C: (a) recession rate; (b) limiting oxide thickness; and (c) time constant*

*Figure 26: (a) Temperature calibration curves for various furnace temperatures and water flow rates. The inset in the bottom left corner shows the tip of the capillary with an outer diameter of 3 mm with the thermocouple. The top right inset shows the evaporation location of the water in the capillary. (b) Vapor jet temperatures and velocities for various furnace temperatures and water flow rates.*

*Figure 27. Wedge-shaped test specimen of SiC after exposure for 20 h in a water vapor jet of velocity 260 m/s and temperature 1160 °C. (a) Before removing from holder used during test: grooves coincide with flow of the edge of the jet. (b) SEM micrograph with superimposed profilometer trace. (c) Optical interference micrograph (white light) from region indicated in*

*(a), showing three sets of interference fringes, from which the surface profile and oxide thickness can be determined.*

*Figure 28: EDX spectra of area shown in Fig. 25 (dark indicating high intensity signal).*

*Figure 29: (a) Higher magnification view from area shown in Fig. 25. (b)Region indicated in (a) from groove at edge of vapor jet. (c) Region indicated in (a) from center of vapor jet.*

*Figure 30: 3D profilometer measurements of specimens subjected to 20 hrs at 1160°C / 1.87 ml/min (a) and 1350°C / 1.87 ml/min (b).*

*Figure31: (a) SiC substrate and (b) $La_2Si_2O_7$ coated substrate after exposure to water impinging jet at 1400C for 16 hours*

*Figure 32 : Microstructures found at different locations on SiC samples exposed to water jet.*

*Figure 33:Profile of SiC substrate after test showing corrosion crater and mounds.*

*Figure 34: (a) Region near the edge of the coating, (b) coating at the edge of the substrate, (c) and (d) details in region (a).*

*Fig. 35. Schematic showing flow of water vapor jet over wedge-shaped test specimen. (flow rate of surrounding argon gas is low, ~ 0.01 m/s, compared with ~ 100 m/s for water jet)*

*Fig. 36. Map showing dependence of erosion rate on flow velocity and temperature for SiC with a continuous oxide surface layer (laminar flow over flat plate, thermodynamic data for $Si(OH)_4$ volatilization from Opila[8])*

*Fig. 37. Plots from Eqs. (1) to (3) comparing erosion of SiC in flowing water vapor and in hydrocarbon combustion (10% water vapor), assuming laminar flow over a flat plate and volatilization of $Si(OH)_4$: (a) steady-state recession rate, (b) limiting oxide thickness, and (c) time taken to reach steady state. Conditions corresponding to several test facilities, including our high speed water vapor jet, are indicated and compared with typical conditions for industrial turbine engines and rocket nozzles.*

# 3 Introduction

The assessment of new compounds for application as high temperature coatings is often limited by the difficulty of producing coatings of controlled composition using conventional methods. Pulsed electron-beam ablation had the potential to avoid this limitation. The use of ablation rather than melting and evaporation avoids changes in composition associated with differing evaporation rates of constituents in a molten target. The use of electrons rather than eximer laser radiation (as in conventional laser ablation methods) enables ablation of materials that do not couple well to the laser because they are partly transparent at the laser wavelength or reflective. Coating compounds of interest included rare–earth phosphates and silicates.

Rare–earth phosphates have a combination of properties (high temperature stability, compatibility, thermal conductivity, and corrosion resistance) that make them of interest for thermal barrier coatings.[1] Our previous experiments with conventional electron beam and laser deposition showed that $LaPO_4$ could be deposited in crystalline form on a heated substrate, although the deposition technique did not allow adequate control of composition. The aim of the present program was to deposit coatings of $LaPO_4$ with controlled compositions and microstructures to allow assessment of their effectiveness as thermal barrier coatings. The deposition conditions used for the pulsed electron beam ablation were investigated with the objective of forming a crystalline columnar microstructure, mimicking the strain-tolerant microstructure of state-of-the-art $ZrO_2$ coatings.

Silicon-based ceramics (SiC and $Si_3N_4$) and their composites are candidates for structural components for hot sections of heat engines and in heat exchangers. However, combustion environments contain large amount of water vapor which has been shown to lead to more rapid degradation than in dry oxygen.[2] Rare-earth silicates have high temperature properties potentially suitable for environmental protection of Si-containing materials in combustion environments.[3] Our initial interest was in the disilicate compounds of the form $X_2Si_2O_7$ (and especially $La_2Si_2O_7$), since at least in certain cases such as $Sc_2Si_2O_7$, they are known to form readily. The aim of the experiments was to deposit coatings of $La_2Si_2O_7$ by pulsed electron beam ablation, with controlled compositions and microstructures to allow assessment of their effectiveness as environmental barriers in high temperature water containing environments.

The assessment of new compounds for use in combustion environments is also limited by the difficulty of measuring their resistance to degradation in representative environments. In parallel with the coating deposition studies, we developed a small scale economical technique to replicate the corrosion from water vapor in turbine engines. We also evaluated the corrosion resistance in sulfate and vanadate salts for $LaPO_4$.

# 4  Pulsed Electron Beam Ablation

### Description

The ablation of a target by electrons requires pulses of high current density with relatively low accelerating voltage (below ~15 KeV) so as to restrict the penetration depth. A method for achieving this by using space charge effects to overcome the mutual repulsion of the electrons was developed at the University of Erlangen[4] and has been improved during the past ten years in several laboratories.[4-8] Recently, Neocera, a company that sells laser-ablation equipment, has produced a commercial instrument based on the German work. The instrument is much smaller, lower in cost, and less complex than conventional EB-PVD systems.

The pulsed electron beam source (referred to as a channel-spark system) consists of a trigger tube, a modified hollow cathode and a dielectric acceleration tube (Fig. 1), all filled with low-pressure gas. The trigger generates a plasma burst that diffuses into the hollow cathode. The hollow cathode is activated and ionizes the gas under a voltage of a few kV causing an electron avalanche. Because of the cylindrical cathode geometry, the electrons are accumulated on the axis. The electrons are then accelerated through a small-diameter channeling tube, with the deposition chamber acting as the anode.



*Figure 1: Pulsed electron beam source and power supply*

An electron beam with low accelerating voltage (up to 15 kV) and very high current density (up to ~$10^5$ A/cm$^2$) is formed. The pulse duration is about 100ns and the repetition rate between pulses is in the range 3-40 Hz (note: our system was limited to 10Hz). The beam size is of the order of 1 to 3 mm. For accelerating voltages in this range the penetration of electrons into the target material is limited and the beam energy is transferred to atoms within a few-microns of the surface. It is estimated that for low conductivity material, ~50% of the beam energy is transferred to the vapor cloud and only a few percent is absorbed as heat. Rotation/translation of the target ensures a uniform erosion of the target and further heat dissipation.

A vacuum chamber was designed and built at RSC (Figure 2A). The chamber is a modified version of the basic design provided by NEOCERA to accommodate different target and

substrate configurations. Figure 2B indicates some of the parameters that control the evaporation and deposition process. Two substrate configurations were developed in the course of this investigation: a flat motionless heater plate and an original heater accommodating rotating cylindrical substrates.
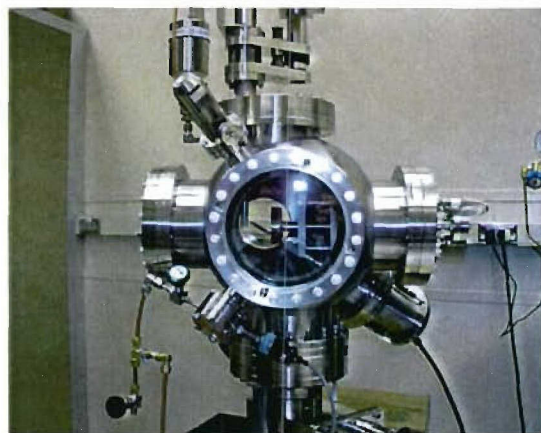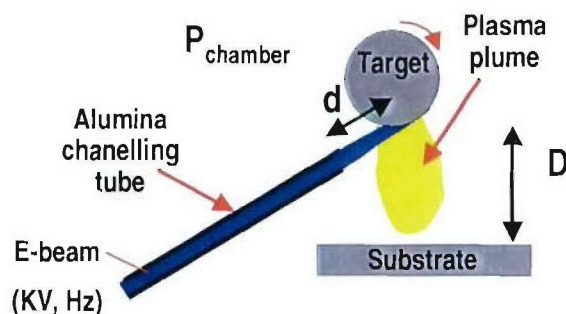


(A)                                                  (B)

*Figure 2: (A) Pulsed Electron Beam chamber, (B) Schematic indicating some of the main parameters (D is target to substrate distance, d is gun tip to target distance).*

## Experimental

For initial investigation of the role of some of the deposition parameters, coatings of alumina and lanthanum phosphate were produced from cylindrical targets of diameter ~10-mm, which were rotated about their axis and translated along the axis over a distance of 0.5 cm to 1 cm so that the beam followed a helical path on the target surface. The distance between the tip of the alumina tube of the gun and the target was set between 5 and 10 mm. This parameter controls the beam size (i.e., approximately 3 mm) and therefore the beam energy density on the target. It is expected that if the distance is too small, spurious effects such as ejection of molten droplets may occur, while if it is too large, the power density may not be sufficient to ablate all elements equally. The distance between the target and the substrate controls the uniformity of the coating. The distance was set between 35 and 65 mm. The substrates were either glass or polished FeCrAlY. In some cases, the FeCrAlY substrates were oxidized to develop a thin (~1 μm) layer of alumina. The substrates were left at ambient temperature in this first series of experiments. The targets were produced by sintering powers synthesized in our laboratories.

The chamber was first evacuated using a mechanical pump and a turbomolecular pump. The pressure was stabilized at ~ 0.03 mTorr (4 mPa). The chamber was then partially closed and oxygen was bled into the chamber by adjusting the flow rate such that the oxygen pressure was stable between 10 and 15 mTorr (1.3 to 2 mPa). The oxygen valve is tuned during the deposition to keep constant the chamber pressure. The oxygen pressure is slightly higher than those used in our previous electron beam deposition experiment at UCSB (i.e., 5 mTorr) and is believed to help control the oxygen stoichiometry in the coatings. A chamber pressure above 15 to 20 mTorr would reduce the pulse energy in our system. The triggering voltage of the gun is the primary

9

control of the pulse energy. The voltage was set at 15 to 16 KV corresponding to a pulse energy of 0.3 to 0.4 J. Finally, the frequency of the pulse and the duration of the deposition determined the deposition rate and final thickness of the coating. The frequency was kept constant during a single run and was raised from 1 Hz to about 6 or 7 Hz during the course of the investigation. The deposition lasted between 15 and 60 minutes.

## Stationary heated target

The deposition process, as monitored through the view port showing the plasma plume in front of the substrate holder, is shown in Fig.3. Examples of coatings deposited on the different substrates (revealed by the discoloration on the substrate surfaces and fringes indicating variation in coating thickness) are shown in Fig. 3b.
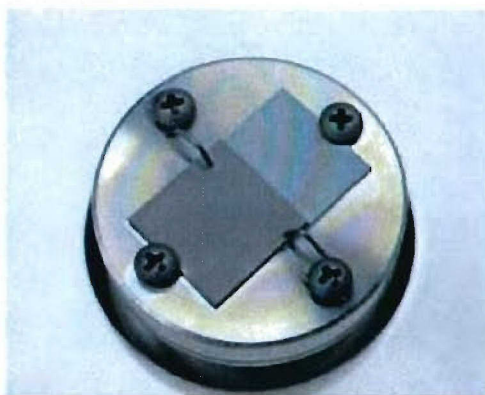


(A)                    (B)

*Figure 3: (A) Flash observed during the interaction of the beam pulse with the target, forming a plasma plume in front of the substrate holder (B) Coated FeCrAlY and glass substrates set on substrate holder.*

## Rotating stage

The growth of an oriented columnar structure in zirconia coatings by EBPVD is largely due to the rotation of the substrate during deposition. Our previous work using traditional EBPVD has shown that such a structure also develops readily when depositing La-P-O composition on a rotating substrate.

Figure 4 shows the configuration of the heater with the rotating substrate and the target during ablation. Alumina tubes of 1-inch diameter were used as substrates. The tubes had a very large grain size (~20 microns) allowing easy discrimination between the morphology of the coating and that of the substrate. Several shields surrounded the substrate to limit heat losses except in front of the target where a window of dimensions ~1"x1" was cut to allow the incoming flux of material from the target to deposit onto the substrate. The substrate rotation was 10 rpm and the temperature was monitored using two thermocouples dragging on the surface of the rotating substrate, one placed in the front window and another in the back beneath the shields. A variation of two to three hundred degrees was noted between these two locations. Both temperatures are referenced later in this report.
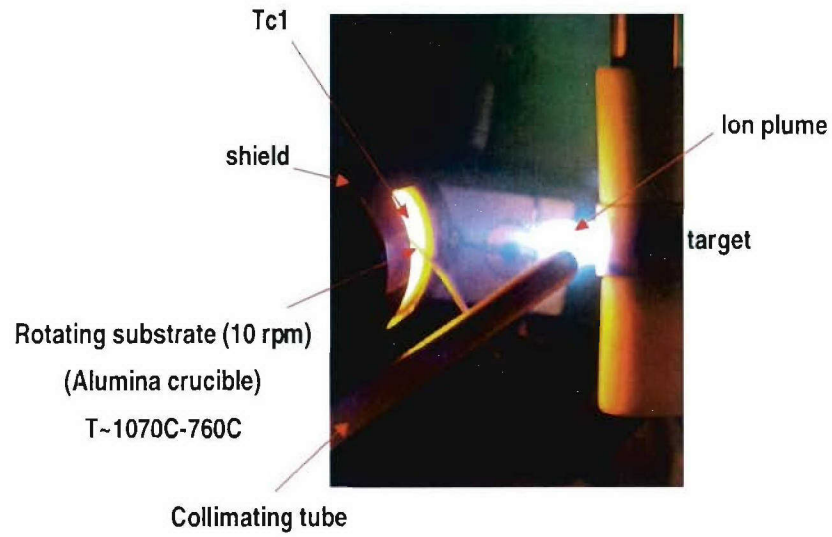
*Figure 4: Configuration of pulsed e-beam deposition with a rotating substrate at thigh temperature.*

# 5   Al$_2$O$_3$ and ZrO$_2$ coatings

**Deposition of Al$_2$O$_3$**

The first trials of the pulsed electron beam ablation were performed with an alumina target (Figure 5 and 6). Low pulse frequency and short deposition time resulted in the formation of small islands of alumina on the substrate. With faster pulse rates and longer times a continuous film was deposited (Figure 6). The coating did not spall after deposition but scratching the surface with a sharp tool debonded the film. Small spherical droplets on the film surface suggested the presence of some liquid droplets in the ablation plume.
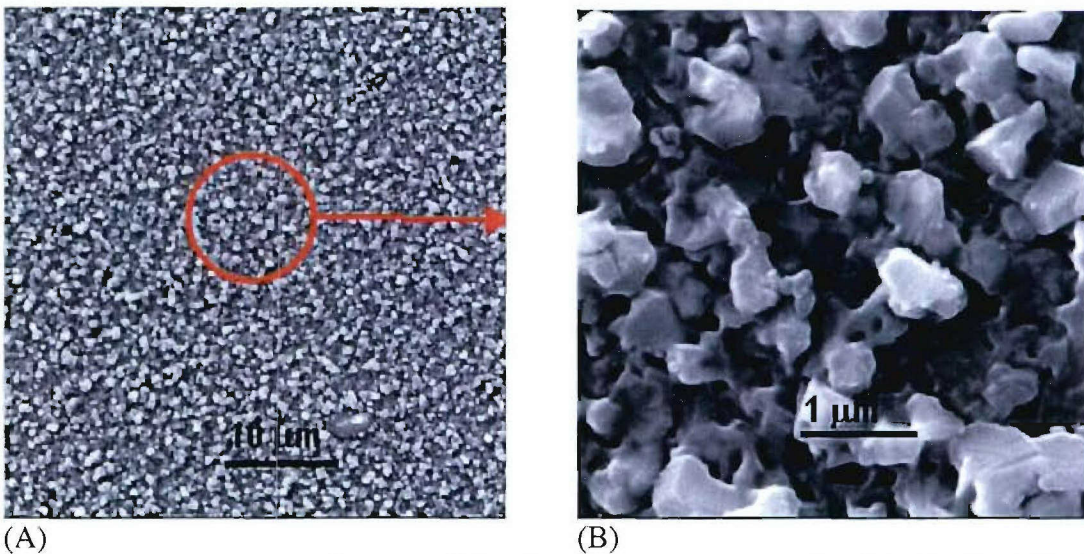


(A)                                                    (B)

*Figure 5: (A) Low magnification of the alumina coating on oxidized FeCrAlY (1Hz, 15 min.), (B) alumina islands deposited on the substrate.*
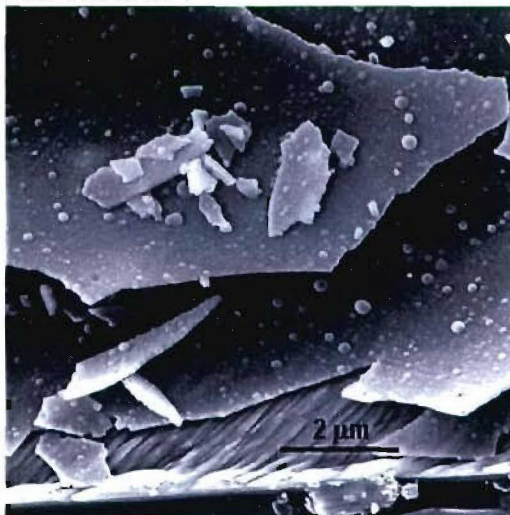


*Figure 6: Continuous alumina coating deposited on polished FeCrAlY substrate (3 Hz, 40 min.). The coating was spalled by scribing the surface using a sharp steel tool.*

## Y-ZrO$_2$ coatings

Coatings of Y-ZrO$_2$ were deposited using the pulsed electron beam system on FeCrAlY substrates (polished and oxidized) to provide a comparison with coatings formed by conventional e-beam deposition (EBPVD). Coatings formed on substrates heated to 500 °C and 800 °C were crystalline with dense columnar structure similar to typical microstructures formed in the initial stages of EBPVD. When the coated substrates were bent around a sharp radius, multiple parallel cracks formed normal to the coating without causing spalling (Fig. 7), thus indicating that the coatings were strongly bonded.
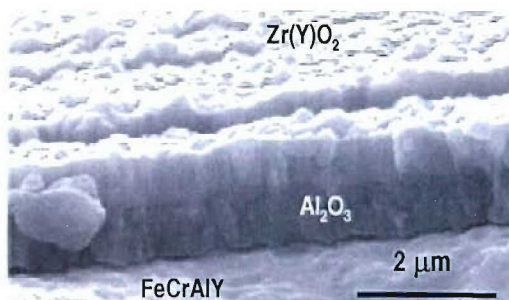


*Figure 7: Y-ZrO2 coating formed by pulsed e-beam deposition on pre-oxidized FeCrAlY substrate: cracks normal to coating were formed by bending the coated substrate around a sharp radius.*

# 6 LaPO$_4$ Coatings

**Stationary target**

Coatings were first deposited using a stoichiometric LaPO$_4$ target at room temperature. Within the range of pulse conditions available, the fastest pulse frequency and the longest duration led to the formation of continuous films on the various substrates tested. The films appeared to consist of small clusters. The thickness of the films reached a few microns (Figure 8 and 9).

Analysis of the films by EDS (Energy Dispersive Spectroscopy) showed that the composition was lanthanum rich. Analysis by X-ray diffraction could not directly confirm this result, although the main peaks of several lanthanum-rich phases (such as La$_7$P$_3$O$_{18}$) were present (Figure 10). In our previous study with conventional e-beam deposition, coatings of lanthanum phosphate on low temperature substrates were poorly crystallized. This cluster morphology may change with a substrate held at higher temperatures. However if preserved, it may increase the defect structure of the coating and hence its insulating properties.
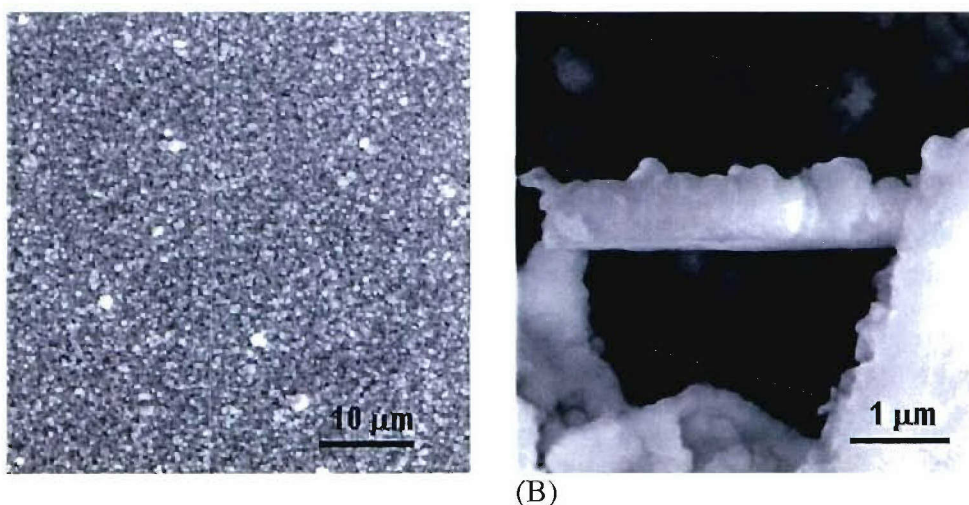


(A)                                    (B)

*Figure 8: (A) Lanthanum phosphate coating on an oxidized FeCrAlY substrate (~5 Hz, 30 min.), (B) cross-section view of the coating after spallation of the coating after scribing the surface.*
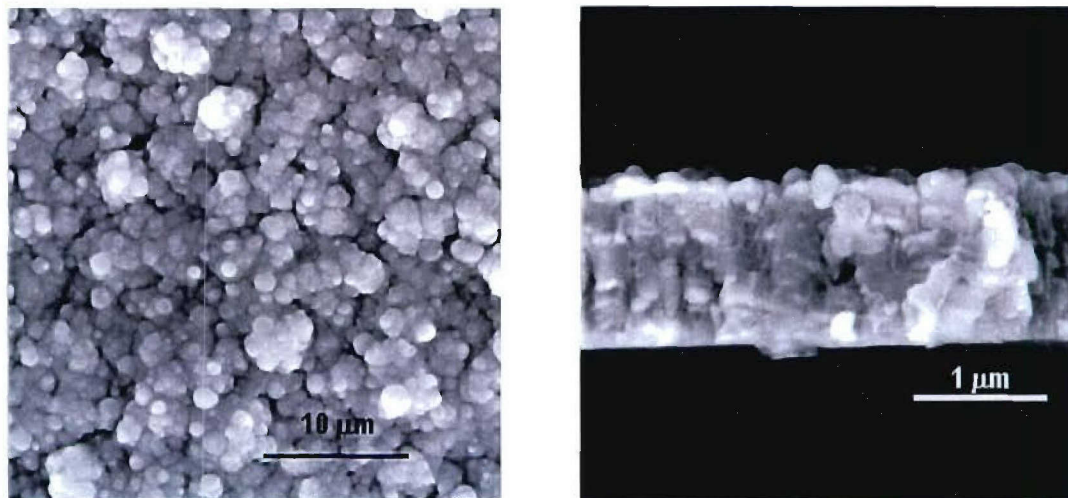
*Figure 9: (A) Lanthanum phosphate coating on an oxidized FeCrAlY substrate (~7 Hz, 60 min.), (B) cross-section view of the coating after spallation of the coating after scribing the surface.*
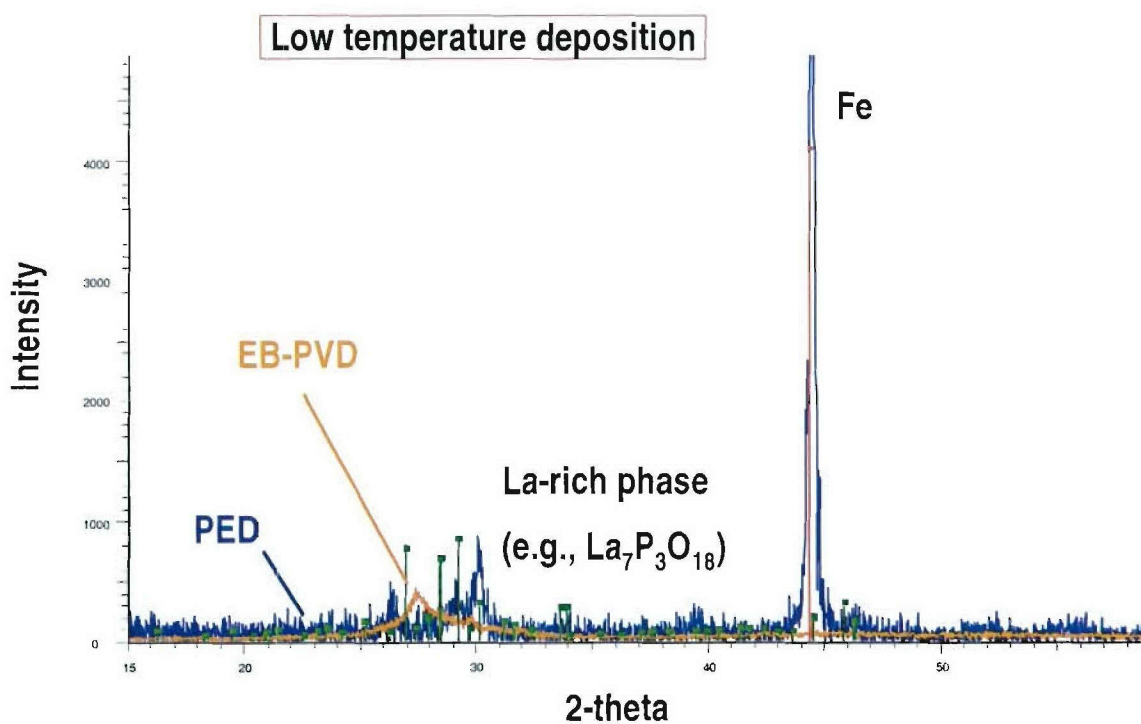


*Figure 10: X-ray diffraction of lanthanum phosphate coatings deposited by EBPVD and PED on low temperature substrates.*

At higher temperatures, the general morphology of the coatings (Fig.11a) was independent of the temperature of the substrate during deposition. However, the degree of crystallization was

sensitive to the deposition temperature: coatings deposited at room temperature were amorphous, whereas coatings deposited at temperatures above ~800 °C were crystalline (Fig. 11b). X-ray analysis indicated that the crystalline coatings formed under a range of conditions contained both La-rich ($La_3PO_7$) and P-rich ($La_2P_4O_{13}$) compounds, whereas the target phase, $LaPO_4$, was not formed. Overall, the coatings contained a higher ratio of La:P than in the target (as measured using EDS), thus indicating that even with an ablation technique, the loss of P during deposition is a factor that must be taken into account.
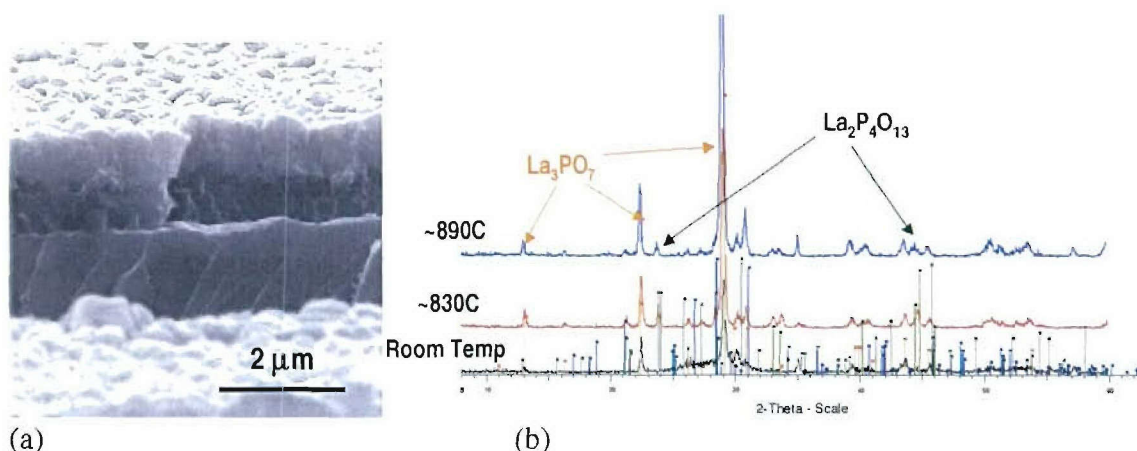


*Figure 11. (a) La-phosphate coating formed by pulsed e-beam deposition on pre-oxidized FeCrAlY substrate. (b) X-ray diffraction data from coatings deposited on substrates heated to temperatures indicated.*

**Rotating substrate**

One of our primary reasons for using a pulsed e-beam system was to improve the stoichiometry of deposited $LaPO_4$ coatings. However, the coatings deposited initially using a stationary target of stoichiometric $LaPO_4$ were always overall rich in lanthanum. In some cases, the coatings consisted of a majority of La-rich phases (e.g., primarily $La_3PO_7$) mixed with some P-rich phases (e.g., $La_2P_4O_{13}$). Several measurements were made in an attempt to understand the origin of the non-stoichiometry.

The first approach was to study the surface of a target after a deposition run. The microstructure of the surface consisted of grains with rounded edges suggesting some exposure to very high temperatures. It is not possible to know whether the surface was molten. Composition analysis of the surface by EDS revealed excess lanthanum, suggesting a preferred loss of phosphorous due to the high temperature exposure. This would require temperatures very close to the melting point of $LaPO_4$. Similar behavior was observed previously with targets of $La_2Si_2O_7$.

The aim in pulsed laser beam deposition is to make use of short pulses of high energy, so that the beam energy is absorbed within a small depth from the surface, leading to ablation without extensive heating of the target, rather than melting and evaporation as in conventional EBPVD. The observations of the target surface discussed above suggest that significant heating occurred, sufficient to cause partial decomposition. In an attempt to reduce the amount of heat conduction into the solid, use of a porous target of $LaPO_4$ was investigated. The resulting coatings deposited on a rotating alumina substrate at temperatures of 670 - 980 °C and 750 - 1070 °C are shown in Fig. 12. The coatings are very thin and nodular, with no evidence of columnar growth detected.

16

The composition of the coating was still very La-rich and X-ray diffraction analysis indicated the formation of a well crystallized $La_3PO_7$ phase (Figure 13). The porous target did not solve the stoichiometry problem. It should also be noted that even though fluctuations in the plume composition may occur due to the modification of the surface composition, steady-state evaporation should be on average stoichiometric.
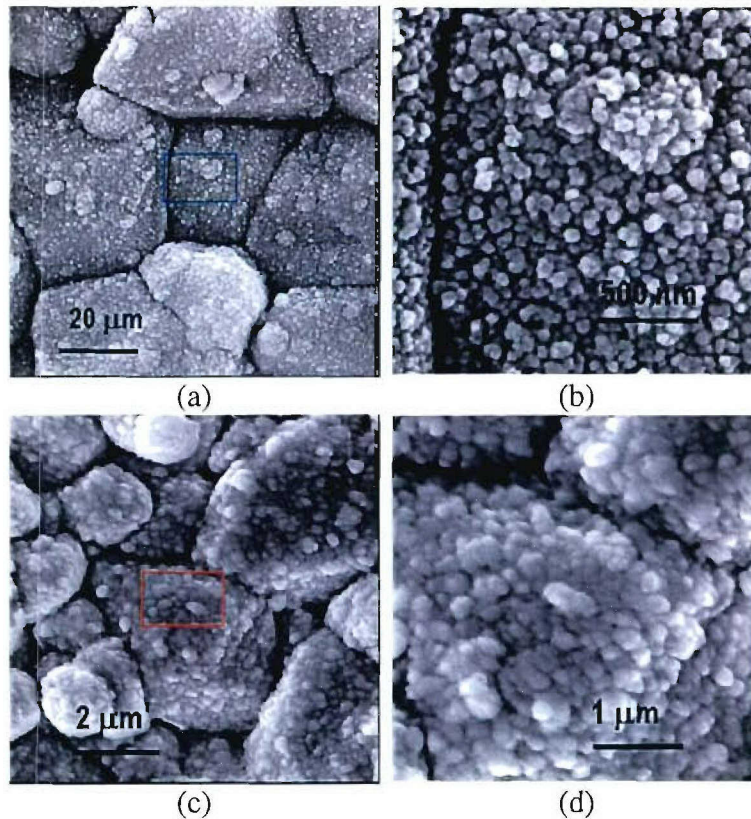


*Figure 12: Microstructures of $La_3PO_7$ deposited coatings on rotating substrate of $Al_2O_3$ with substrate temperatures of 670-980 °C (a and b) and 750-1070 °C (c and d)*
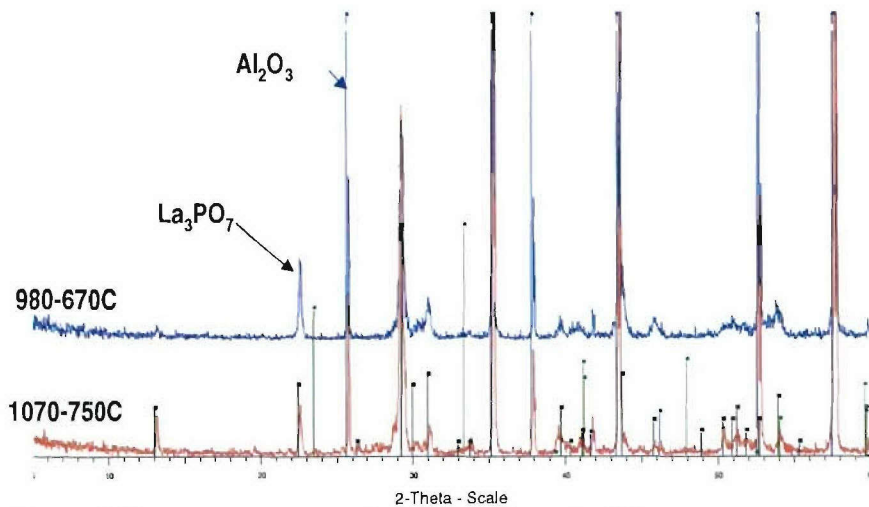


*Figure 13: X-ray diffraction patterns of coatings deposited from a porous target of $LaPO_4$.*

17

# 7  La-silicate coatings

Coatings of La-silicate were deposited using the pulsed electron beam system on stationary SiC substrates held at various temperatures. The targets were produced by sintering powders synthesized in our laboratories at temperatures of 1550°C and 1600 °C. The powders were mixed so as to give La:Si ratio of 1:1, as in the disilicate compound. The sintered materials contained an oxy-apatite phase ($La_{9.33}(SiO_4)_6O_2$) in addition to the disilicate phase ($La_2Si_2O_7$) and porosity (about 20%, beneficial for thermal shock resistance and to lower thermal conductivity). From SEM and x-ray analysis we could not detect a silica-rich phase to balance the La-rich oxy-apatite, although the possible existence of such a phase is not eliminated by these observations.

The coatings were all dense and showed varying degrees of columnar microstructure (Fig. 14). Coatings deposited at room temperature were amorphous, as expected. Crystallized coatings were produced both by deposition on heated substrates and by heating of coatings formed at room temperature. In both cases the crystallization was complete at temperatures above 800 °C to 900 °C. In both cases the only phase observed by x-ray diffraction was the oxy-apatite ($La_{9.33}(SiO_4)_6O_2$): the disilicate phase ($La_2Si_2O_7$) was not detected in any of the coatings. EDS analysis indicates an overall La:Si ratio in the coatings consistent with the oxy-apatite phase and lower than in the target. Analysis of the targets after deposition showed a thin amorphous, La-rich surface layer. These results indicated that the pulsed e-beam causes some melting in addition to ablation, with some loss of Si occurring during deposition.
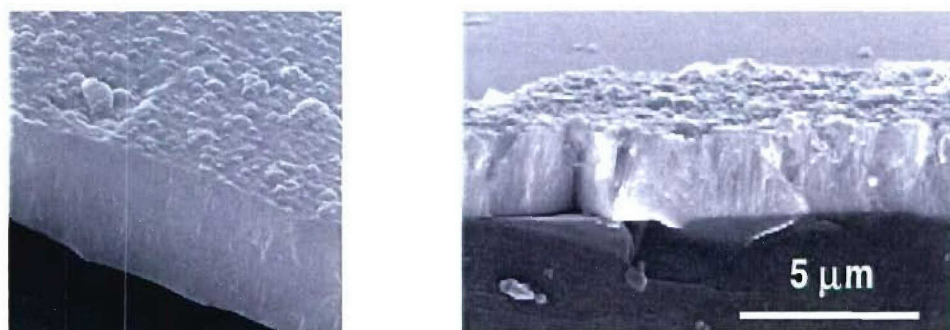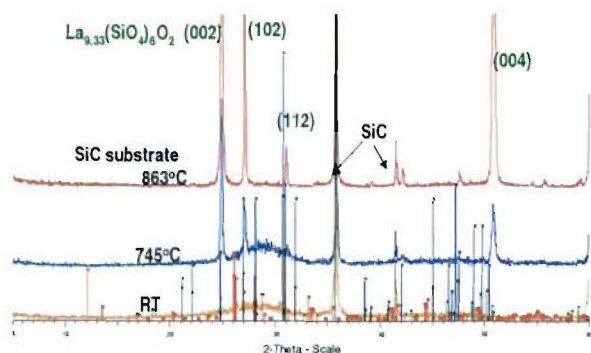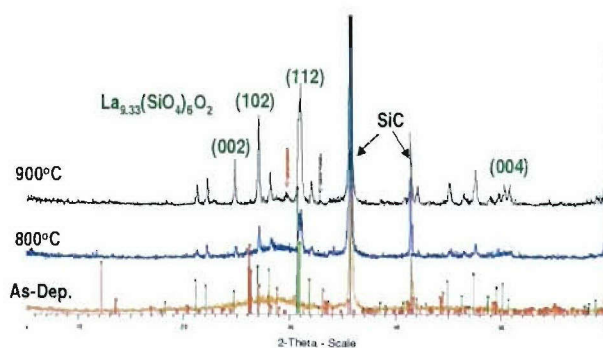


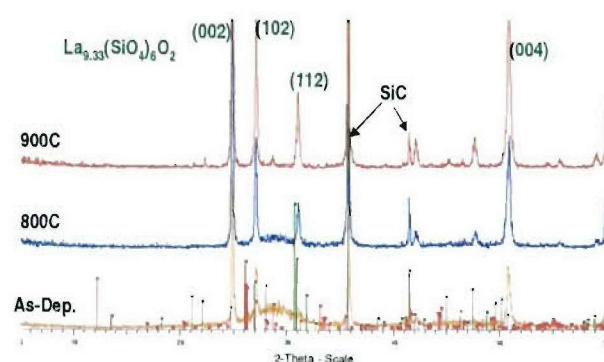*Figure 14: La-silicate coatings deposited on substrates heated to (a) 863 °C and (b) 883 °C*

The oxy-apatite phase showed a strong preferred orientation ((001) parallel to surface) in coatings deposited on heated substrates (Fig. 15a) but no preferred orientation in coatings that were crystallized by heating the amorphous structure deposited at room temperature (Fig. 15b). However, the preferred orientation was preserved after heating partly crystallized coatings deposited at intermediate temperature (780 °C) to higher temperatures (Fig. 15c). This additional heating caused further crystallization, presumably by a templated grain growth mechanism.

.

(a)



(b)



(c)

*Fig. 15. X-ray diffraction data from La-silicate coatings formed by pulsed e-beam deposition: (a) substrate heated to temperatures shown; (b) deposited on substrate at room temperature then heated to temperatures shown; and (c) deposited at 780 °C then heated to temperatures shown.*

The lanthanum oxy-apatite phase observed here is not shown on the standard phase diagram[9] (Fig. 16a), which shows only 1:1, 2:3, and 1:2 compounds ($La_2O_3$:$SiO_2$) in this region. However its formation is consistent with several recent studies. One showed that in the Nd silicates the 7:9 oxy-apatite phase melts congruently and claimed that the 2:3 phase was mistaken in earlier work and really does not exist (was a mixture of 7:9 oxy-apatite and 1:2 disilicate phases). Navrotsky et al[10] measured heats of formation of various rare-earth oxy-apatite compounds. Comparison of these with data for the RE disilicates indicates that the oxy-apatite phase becomes increasingly more stable relative to the disilicate phase as the RE size increases (lanthanum oxy-apatite being the most stable). Extrapolation of this trend to the small RE silicates would suggest the disilicate compound would become the more stable for RE ions smaller than Yb. The smallest member of this family, Sc, is known to act as a scavenger in silicate minerals to form the disilicate phase (thortvetite). The very low formation enthalpy of La oxy-apatite may suggest a high resistance to water vapor attack.
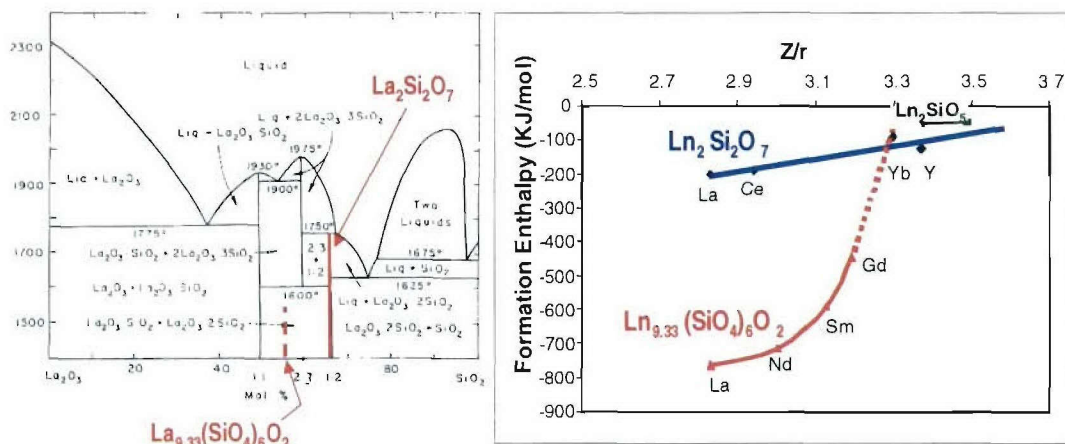
*Figure 16. (a) Phase diagram for La$_2$O$_3$ – SiO$_2$ system.[9] (b) Formation enthalpy for various rare-earth silicates [10]*

# 8 Understanding the stoichiometry issue

In the pulsed electron beam system, material is ablated from the target in a plume with maximum intensity normal to the surface. The substrate intersects the central portion of the plume collecting a fraction of the ablated material. A simple experiment was designed to map compositional variations within the plume and test whether variations in the deposited coatings might originate from non-uniformity of the plume. This involved placing unheated Mo foils on each side of the substrate, as shown in Fig. 17, and analyzing the amount of deposited lanthanum and phosphorous by EDS as a function of distance along the foils. The results in Fig. 18 show a clear difference in deposition patterns for the La and P, with the composition being La-rich at the target and P-rich at distances greater than ~ 30 mm from the target. The La/P ratio on the target and in its immediate vicinity on the foil was ~ 2.5 to 3, correlating with the observed $La_3PO_7$ compound on the target surface. The La/P ratio decreased monotonically to ~0.6 at distances beyond about 40 mm from the substrate.
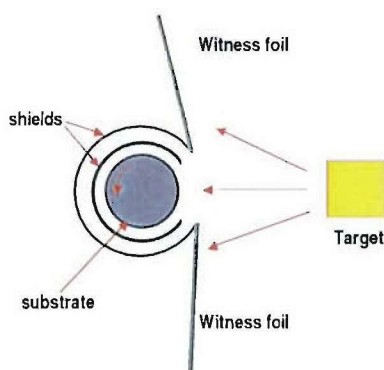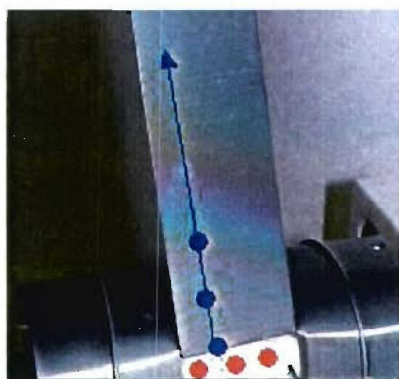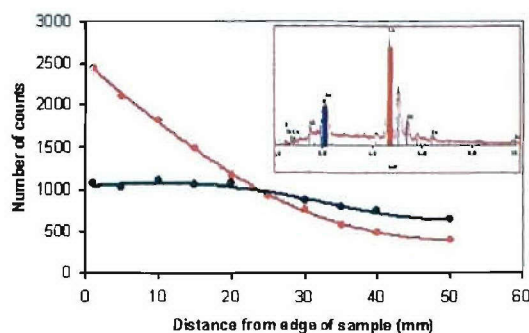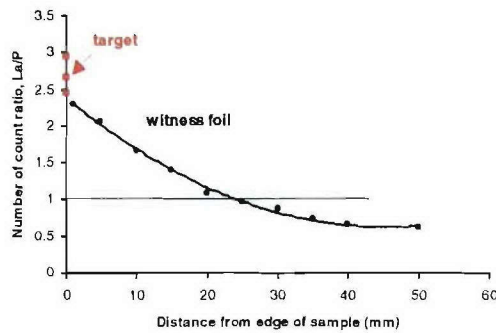


*Figure 17: Configuration of witness foils placed on each side of the substrate.*



(a)

(b)

(c)

*Figure 18: (a) Location of measurement along the foil and on substrate, (b) analysis of peak height for P and La, (c) La/P ratio on substrate and along the foil length.*

The compositional variation across the plume may be an intrinsic phenomenon related to the large difference in mass of the La and P species. If the transfer of energy of the beam is similar for both La and P atoms, then the ratios of their speed and momentum are 0.5 and 2 respectively ($M_{La} \sim 4\ M_P$). As the vapor moves away from the target, collisions in the vapor phase will occur and the difference in mass and momentum may disperse the lighter, faster P species from their original path.

Three potential approaches were envisioned for avoiding or compensating for the intrinsic demixing of La and P in the vapor phase:
1. modify the target composition by increasing the amount of P
2. collimate the plume using a gas jet (e.g., He or $O_2$)
3. use two targets (and 2 beams) matching the speed of the two species.

The first solution was implemented since the other two would require major changes in our chamber configuration. A target was fabricated with about equal weights of $La_2O_3$ and $P_2O_5$ (mole ratio P/La ~2.3). This composition was chosen to give a coating with $LaPO_4$ composition based on the amount of phosphorus lost during our previous experiments using a stoichiometric target (i.e., $La_3PO_7$ composition from a $LaPO_4$ target) (Figure 19). Witness foils were positioned to monitor the vapor field around the substrate.
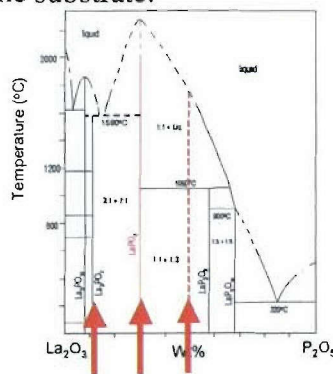


*Figure 19: Phase diagram of $La_2O_3$-$P_2O_5$, indicating the composition of $La_3PO_7$, $LaPO_4$ and 50 $La_2O_3$-50 $P_2O_5$ respectively from left to right.*

The profiles of La and P vapor concentrations on and around the substrate are shown in Fig. 20. The ratio of La:P was unity (stoichiometric value for $LaPO_4$) on the substrate, but decayed rapidly with distance beyond the edge of the substrate. The profile of the lanthanum was similar to that of the previous experiments but the P concentration profile exhibited a maximum at about 1 inch from the edge of the substrate. This behavior corroborated the demixing hypothesis and underlines the difficulty of controlling the stoichiometry of the coating over large distances.
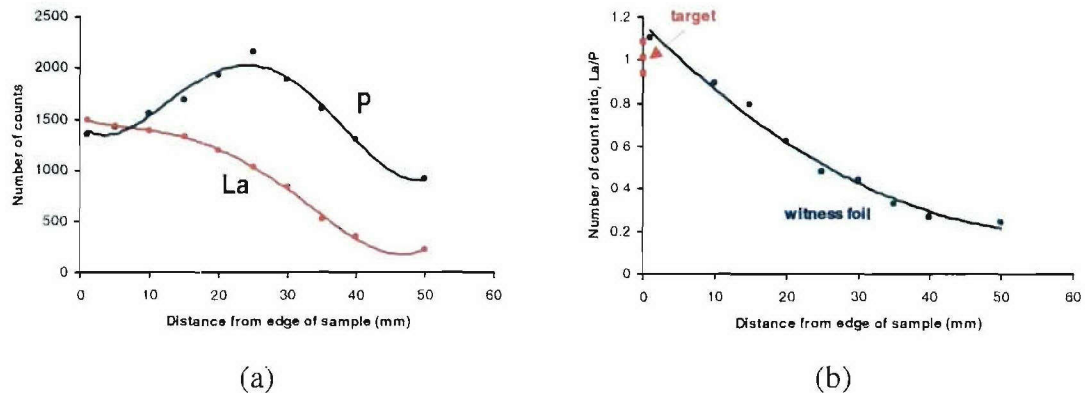


(a)                                           (b)

*Figure 20: (a) Concentration profile of La and P along the foil, (b) La/P ratio along the foil and on the target.*

The microstructure of the coating deposited from the P-rich target is shown in Figure 21. Even though the temperature was high (750 °C-1050 °C), the microstructure consisted of accumulated small rounded grains and did not develop into a columnar structure. Analysis by X-ray diffraction indicated the presence of monazite (Fig. 21b). However, other P-rich and La-rich phases were also formed, suggesting some more complicated phenomena of deposition at small scale (e.g., small scale vapor composition variations, crystallization kinetics differences). The use of a P-rich target gave a secondary advantage of increasing the deposition rate, presumably due to a lowering of the melting/sublimation point of the target composition (Figure 19).



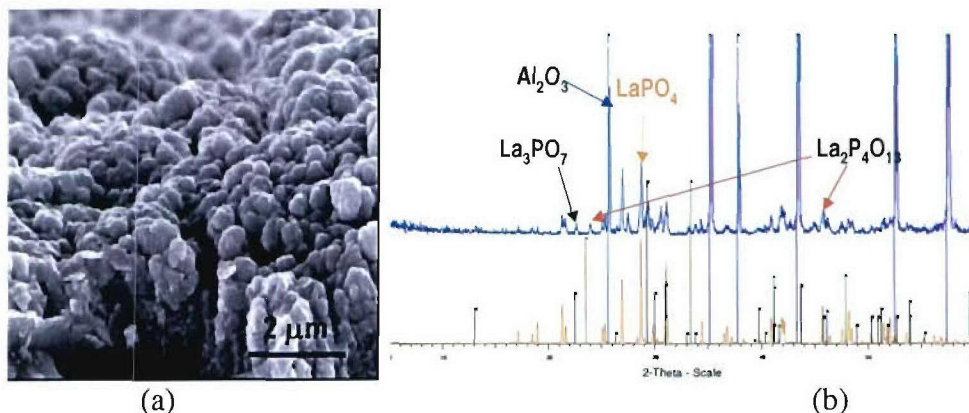(a)                                           (b)

*Figure 21: (a) Microstructure of coating deposited from P-rich target. (b) X-diffraction patterns showing the presence of $LaPO_4$, $La_3PO_7$ and $La_2P_4O_{13}$.*

In conclusion, the deposition of $LaPO_4$ on a hot, rotating substrate was achieved using Pulsed Electron Beam ablation with a P-rich target. However, the study showed that: (i) the current

instrument does not allow deposition rates that are suitable for the processing of coatings of hundreds of microns thickness; (ii) although the 1:1 La:P stoichiometry of $LaPO_4$ was achieved overall on the substrate, local variations of stoichiometry persisted, as shown by the presence of both La-rich and P-rich phases; and (iii) columnar growth was not demonstrated, presumably because of the small deposition rate and possibly because the substrate temperature was not sufficiently high.

# 9 Molten salt corrosion

Some preliminary experiments were done to compare the resistance of $LaPO_4$ and $Y-ZrO_2$ to corrosion from molten salts of $NaSO_4$ and $NaVO_4$, which are common impurities in fuel for turbine engines. Both test materials were fully dense fine grained polycrystals: the $Y-ZrO_2$ was a commercial material from Tosoh; the $LaPO_4$ was produced by sintering powder synthesized in our laboratories. This powder was subjected to extensive refinement and testing to eliminate excess P or La.

Several test configurations were explored, since it is known that corrosion can be sensitive to the thickness of the layer of molten salt on a test surface (thin films sometimes being more severe than thick films). In all cases, the test specimens were placed in contact with the salt (solid), enclosed in a double crucible system (new alumina crucibles) with alumina powder in the space between inner and outer crucibles, and heated in a furnace to selected temperatures above the melting point of the salt. Test configurations included: (i) polished surface partly covered with a salt pool, giving a range of conditions from a bare surface exposed to vapor, to surfaces covered with liquid films of varying thickness, (ii) polished surfaces with Vickers indentations, which allow controlled study of the penetration and corrosion around cracks, and (iii) test specimens with drilled holes (several mm in diameter and depth) containing a reservoir of molten salt.

Some of the observations are summarized as follows:
(i) $NaSO_4$ at 650 °C and 900 °C (16 °C and 160 °C above melting point): both $LaPO_4$ and $Y-ZrO_2$ showed etching at grain boundaries, but no large scale corrosion. The degree of etching was slightly greater beneath the molten salt than in regions exposed only to vapor and slightly larger within the central contact area of indentations than in surrounding areas. However, there was no variation of the degree of etching with thickness of molten salt, and no enhanced corrosion around indentation cracks (Fig. 22).
(ii) $NaVO_3$ at 650 °C and 900 °C (20 °C and 270 °C above melting point): severe corrosion of $LaPO_4$ was observed in regions in contact with liquid, leaving graded porous zones of depth ~ 20 $\mu$m at 650 °C and >50 $\mu$m at 900 °C (Fig. 23).
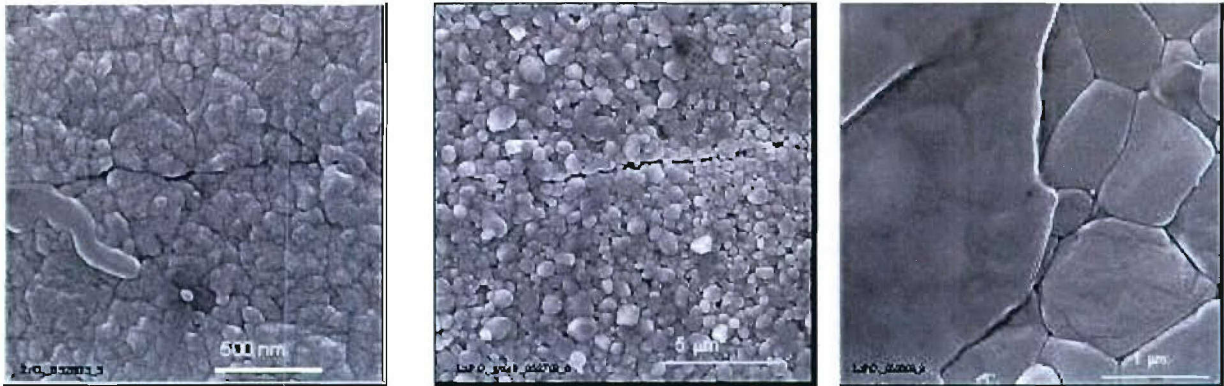
Fig. 22. Etching of polished surfaces by NaSO$_4$ at 1000 $^{\circ}$C: (a) Y-ZrO$_2$, region around indentation crack (horizontal dark line); (b) LaPO$_4$, region around indentation crack (horizontal dark line); (c) LaPO$_4$, region near edge of melt pool.
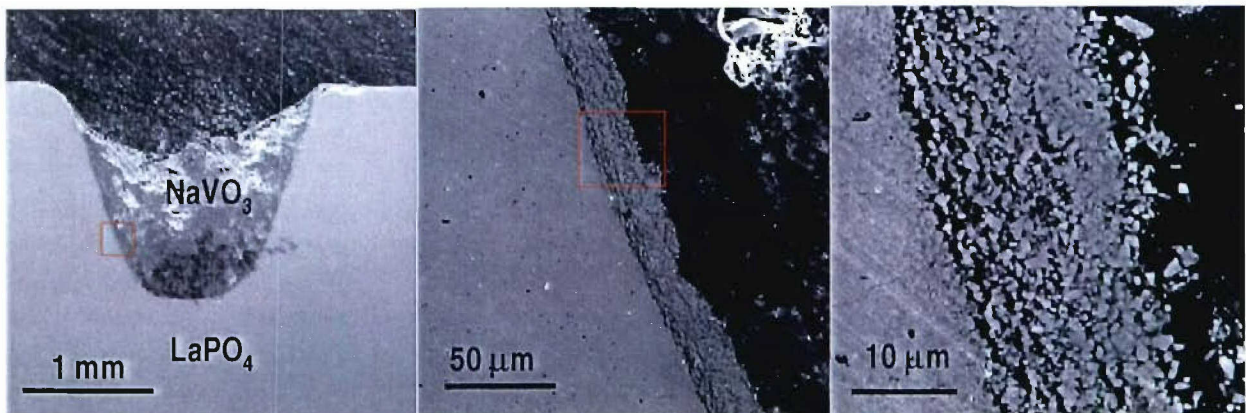


Fig. 23.   Reaction of monazite with NaVO$_3$ salt at 650 $^{\circ}$C (Tm+20 $^{\circ}$C) (a) view of drilled hole with molten salt inside (b) and (c) details of the framed regions in (a) and (b) respectively showing the partial dissolution of the monazite grains into the salt.

# 10  Corrosion by water vapor in combustion environments

## 10.1 Introduction

The sensitivity of silicon-containing ceramics to corrosion by water vapor in combustion environments has motivated efforts to develop environmental barrier coatings consisting of complex oxides that are more resistant than $SiO_2$ to water vapor corrosion.[11-18] However, the data on corrosion rates for other oxide compounds are very limited. The difficulty of measuring the response of developmental coating materials without going to extremely costly engine tests remains a major barrier to development: conditions achieved in laboratory testing typically fall short of engine conditions in their severity by many orders of magnitude.

We have developed an efficient laboratory-scale facility that generates a high speed, high temperature jet of water vapor, which impinges on the surface of a test sample. The conditions generated by the water jet are representative of those experienced in turbine engines in partial pressures, impingement velocities, and erosion rates. The jet is formed by feeding water at a controlled rate into a capillary tube inside a tube furnace (Fig. 24), where the large expansion of vaporization within the confines of the capillary accelerates the jet. With very modest flow rates of liquid water, steam jet velocities typical of flow rates in industrial turbines can be achieved (e.g., the flow of water 2 ml/min into a 1mm-diameter capillary creates a jet at 1300°C and 1 atm pressure with a velocity of ~300 m/s). The partial pressure of water vapor in the 100% steam jet is the same as in an industrial turbine operating at 10 atm total pressure with 10% water vapor. The test set-up, described more fully below, builds on work reported earlier by Ferber[19] who used a capillary to produce a steam jet, although with gas velocities an order of magnitude lower (35 m/s).



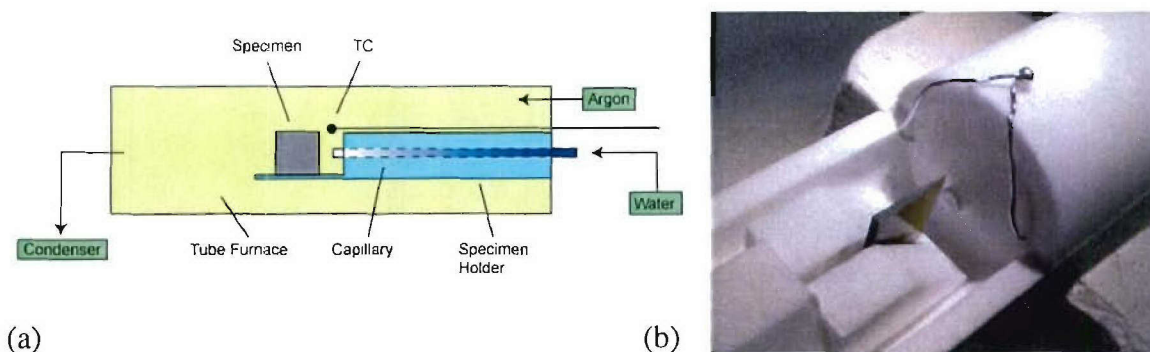(a)                                                            (b)

*Fig. 24. (a) Schematic of water jet test set-up. (b) Photograph showing support fixture and wedge-shaped SiC test specimen in front of the capillary tube.*

The area of the test sample exposed to these conditions is small (~ a few mm diameter). Whereas this is a disadvantage for measuring degradation in the conventional manner through weight

changes, the presence of an unexposed reference surface makes it very convenient for a more direct approach of measuring surface recession.

Two impingement configurations were investigated. In one, the water vapor jet impinged directly on the leading edge of a sharp wedge-shaped test specimen as shown in Fig. 24b, with flow almost parallel to the wedge faces. In the other, the jet impinged on a flat polished surface inclined at angle of $45°$ to the flow.

## 10.2 The $SiO_2$ system: dependence on environmental conditions

Opila and coworkers have provided a comprehensive analysis of the behavior of silica forming materials (SiC and $Si_3N_4$) in flowing gas containing water vapor, under conditions where reaction to form $Si(OH)_4$ dominates at the outer surface and the reaction rate is limited by diffusion of the reaction product through a laminar boundary layer.[20] This involved use of a correlation function for the Sherwood number for flow over a flat plate, which relates the mass flow rate to the Reynolds number (hence to velocity and pressure), the diffusion coefficient, viscosity, and the equilibrium reactant concentration. From these results, combined with analysis of the oxidation reaction at the $SiC$-$SiO_2$ interface, the following expressions were derived for the steady-state erosion rate, the limiting oxide thickness, and the time to achieve steady state:

$$\dot{y}_L = C_1 \frac{v^{1/2} P_{H_2O}^2}{P^{1/2}} \tag{1}$$

$$x_L = C_2 \frac{P^{1/2}}{P_{H_2O}^3 \, v} \tag{2}$$

$$t_L = C_3 \frac{P}{P_{H_2O}^3 \, v} \tag{3}$$

where $v$ is the gas velocity, $P_{H_2O}$ is the partial pressure of water vapor, $P$ is the total pressure, and $C_1$, $C_2$, and $C_3$ are constants dependent on gas properties, reaction enthalpy and temperature. Test data for recession of SiC from several facilities (high pressure burner rig and synthetic combustion gas furnace) were correlated with these expressions and used to calibrate the constants $C_1$, $C_2$, and $C_3$ at a temperature of 1316 °C.

From these results, maps were generated in terms of gas velocity and pressure, which allow ready comparison of conditions achieved in various test configurations and real engines (Fig. 25), as well as some of the limits of the analysis.[20] It is apparent that even sophisticated burner rig facilities (Mach 0.3 burner rig and high pressure burner rig) do not simulate conditions in an industrial gas turbine well: the steady state erosion rates are smaller by a factor of 10 to 100; the limiting oxide thicknesses are larger by a factor of 10; and the times taken to achieve steady state are longer by a factor of 100. The conditions in laboratory furnaces, either with flowing gas or in a special high pressure furnace, are many orders of magnitude further from the turbine conditions.
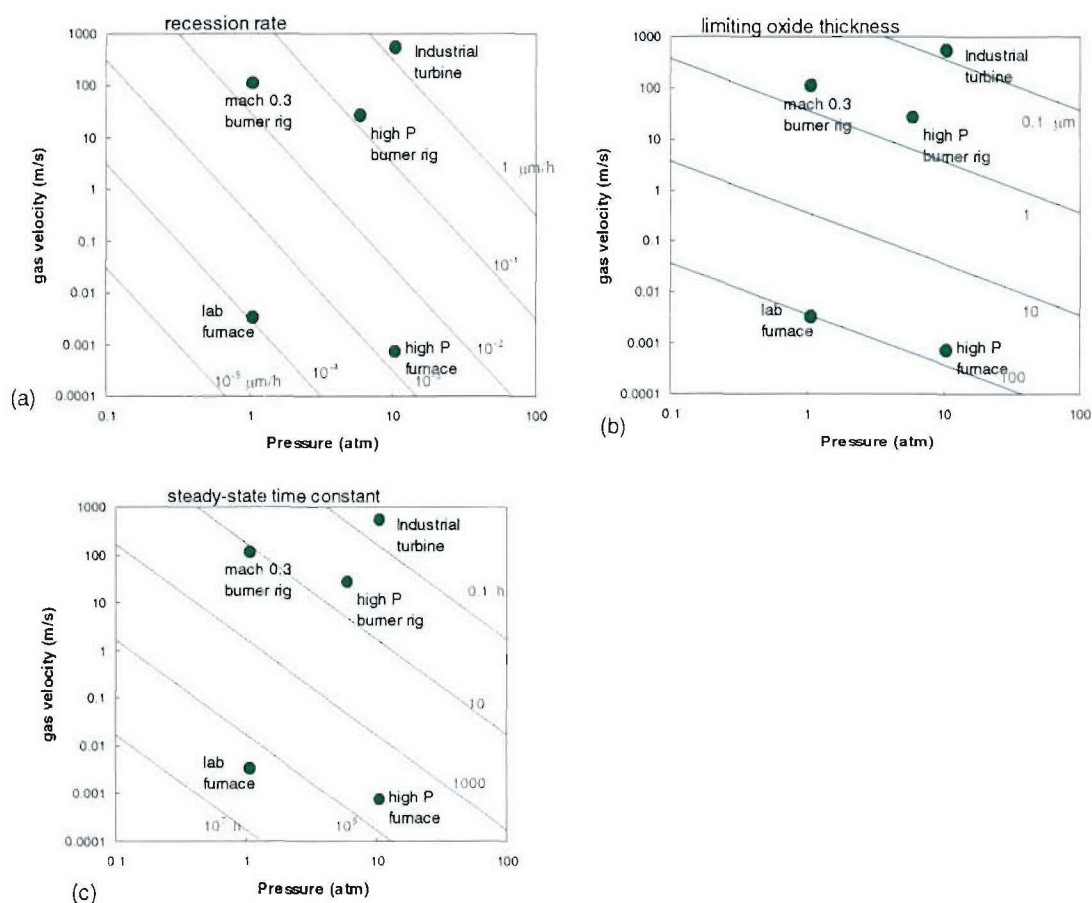
*Fig. 25. Maps of steady-state conditions in terms of gas velocity and total pressure for hydrocarbon combustion at 1316 °C: (a) recession rate; (b) limiting oxide thickness; and (c) time constant*

Closer examination of Fig. 25 suggests limits to the ranges of pressure and temperature over which this erosion mechanism applies. At low gas velocities and pressures typical of laboratory furnaces, the time requires to approach steady state is >10,000 h. In any practical experiment the erosion rates are negligible and the kinetics are dominated by the parabolic growth of the oxide layer. Moreover, the limiting oxide thickness becomes sufficiently large that spalling can occur.

At the other extreme of high velocity and pressure, as experienced in industrial gas turbines, the time to reach steady state is only a few minutes, the erosion rates are high (~1 μm/h) and the oxide thickness is very small (< 0.1 μm). In this case the small oxide thickness may lead to breakup of the oxide layer and a change in the rate-controlling mechanism from volatility of $SiO_2$ to the direct reaction of SiC or $Si_3N_4$ with water vapor. Several possibilities were proposed by Opila:[20] (i) rate controlled by reaction of SiC (or $Si_3N_4$) with water to give $SiO_2$, with the oxide being swept away as soon as it is formed, (ii) "active" volatilization similar to the active oxidation that occurs for $SiO_2$-formers at low partial pressures, where $SiO(g)$ is formed rather than $SiO_2$. In this case, an analogous reaction would be SiC reacting directly with water to give $Si(OH)_4(g)$, without the intermediate $SiO_2$ formation step. Evidence for a transition in behavior

29

to a direct reaction was reported[19,20] for $Si_3N_4$ vanes after exposure in industrial turbines. Evidence has also been seen in our work in another program on SiC in $H_2O_2$ rocket combustion environments with even higher pressures and gas velocities. Because these conditions cannot be readily obtained in a laboratory environment, there is very little understanding of the details of the mechanism. However, there is evidence for greatly accelerated erosion rates in this regime.[19,20]

## 10.3 Experimental method

The experiments were conducted in a tube furnace equipped with a 36" mullite tube. Two flanges accommodate several inlet and outlet attachments for gas and water supply.

A quartz glass capillary with a 1 mm diameter hole is mounted along the center of the tube and connects through the inlet flange to a peristaltic pump, which feeds ultra-high purified water into the system. In order to obtain accurate temperature measurements, a type R thermocouple is routed through the alumina tube and hold either in front of the capillary tip for temperature calibration or on top of the tip for the actual experiments. Additionally, argon is flowed through a second inlet at a rate of 10 cuft/min. The argon and the water vapor are extracted through a single outlet and passed through a condenser before being released into the atmosphere.

The first experimental step consisted of calibrating the temperature of the water vapor jet to various water flow rates and furnace temperatures. The thermocouple bead was placed about 1 mm from the tip of the capillary at the exact position were the actual specimens would be mounted during the experiments. A test matrix including water flow rates between 1 ml/min and 6 ml/min and furnace temperatures between 1300°C and 1500°C was run. The temperatures were recorded after reaching steady state before and after the water was turned on as well as after the water was turned off to ensure that the thermocouple did not degrade during the experiments.

Two experimental configurations of the vapor jet relative to the substrate were tested. SiC plates ($10 \times 10 \times 1$ mm$^3$) cut from CVD thick deposits were polished and placed either with an edge in the flow (i.e., leading edge configuration) or with the large flat face at a ~45° from the flow direction (i.e., flat plate configuration). The leading edge specimens were hand-ground on one side of the plate to form an asymmetric sharp wedge. The specimens were mounted on a specially cut SiC or alumina holder and placed at ~ 5mm from the end of the capillary exhaust. A SiC sample coated with a thin (~1μm) layer of $La_2Si_2O_7$ was also tested in the flat plate configuration.

Four combinations of temperature, water flow rate and duration were used. In the flat plate configuration, the water flow rate was 6ml/min with a nominal furnace temperature of 1400°C and the experiment lasted for 16 hours. In the leading-edge configuration, the water flow rates were 1.87 ml/min for 20 hrs and 12 hrs and 1 ml/min for 20 hrs all at a conducted at a furnace temperature of 1500°C. After the experiments the depth of the erosion has been measured by profilometry and optical interferometry along several lines.

## 10.4 Results

### Temperature calibration

Results of the temperature calibration are summarized in Fig. 26. In the current setup, the length of capillary tube in the hot zone of the furnace is not sufficient to allow equilibration of the temperatures of the water vapor and the furnace atmosphere, so that the temperature of the vapor jet is lower than the furnace temperature by an amount that is sensitive to the flow rate. An estimate of the position at which the liquid water vaporized could usually be obtained from a slight discoloration visible on the inside of the capillary tube after the test run (from contaminants in the water). In the examples shown in Fig. 26a, the distances between this position and the exit of the capillary were approximately 5 and 7 inches for flow rates of 1.0 and 1.87 ml/min, corresponding to a residence time in order of 1 μs. As a result of the increasing temperature difference with increasing flow rate, the velocity of the vapor jet at given furnace temperature does not increase monotonically with the water flow rate (Fig. 26b).
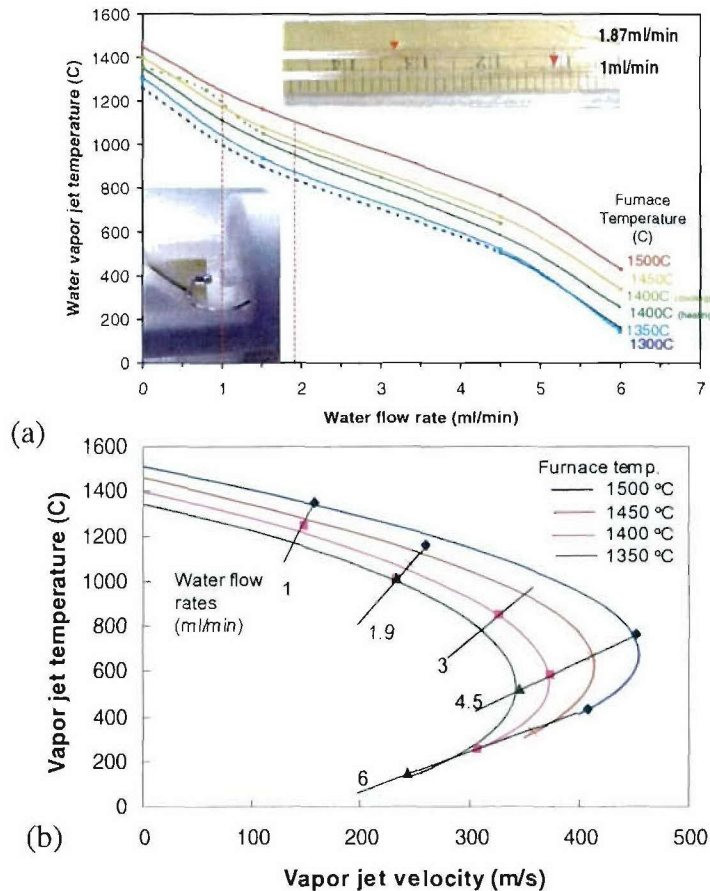


*Figure 26: (a) Temperature calibration curves for various furnace temperatures and water flow rates. The inset in the bottom left corner shows the tip of the capillary with an outer diameter of 3 mm with the thermocouple. The top right inset shows the evaporation location of the water in the capillary. (b) Vapor jet temperatures and velocities for various furnace temperatures and water flow rates.*

31

## Wedge-shaped leading edge specimens

A sharp wedge-shaped SiC test sample is shown in Fig. 27, after exposure for 20 h in a jet of velocity 260 m/s and temperature 1160 °C (furnace temperature 1500 °C). Severe recession occurred both in the position of the leading edge (originally a straight line) and in grooves along the initially flat polished faces of the wedge. The positions of the deepest grooves coincide with flow at the periphery of the water vapor jet. From the profilometer trace shown in Fig. 27b, the recession depth in the central region of the jet flow is ~7 μm, whereas the grooves at the edge of the flow are deeper by a factor of 3 or more (~ 20 μm and 25 μm).
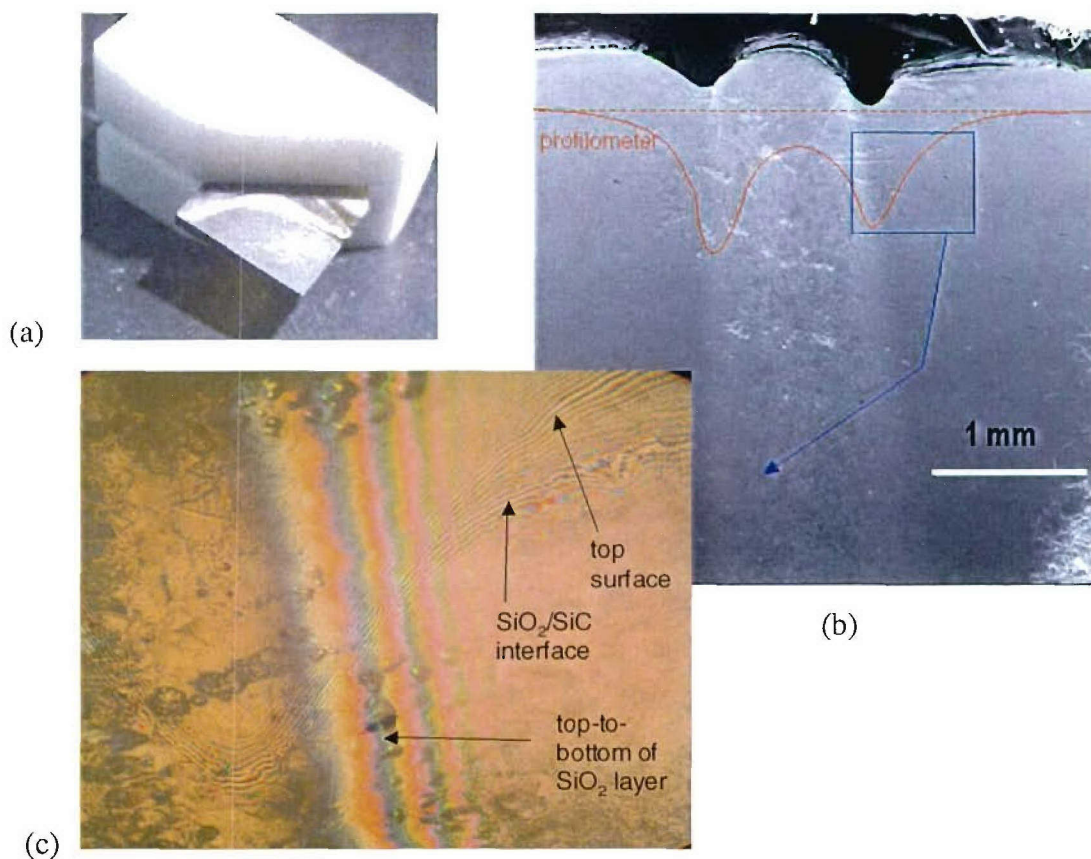


Figure 27. Wedge-shaped test specimen of SiC after exposure for 20 h in a water vapor jet of velocity 260 m/s and temperature 1160 °C. (a) Before removing from holder used during test: grooves coincide with flow of the edge of the jet. (b) SEM micrograph with superimposed profilometer trace. (c) Optical interference micrograph (white light) from region indicated in (a), showing three sets of interference fringes, from which the surface profile and oxide thickness can be determined.

Examination by SEM with EDS analysis indicated that there was continuous $SiO_2$ layer outside the region of jet flow, discontinuous patches of very thin oxide in the central region of the jet flow, and bare SiC in the deep grooves, with no detectable evidence for the presence of oxide.

Elemental maps of silicon, oxygen, carbon and aluminum from the region of Fig. 27b are shown in Fig. 28 (note the absence of oxygen along the groove, reduced oxygen signal at the central region of jet flow, and complementary regions of high and low oxygen and carbon signals). The presence of aluminum outside the region of the jet is indicative of formation and deposition of aluminum oxy-hydroxides by reaction of water vapor in the surrounding gas with the alumina furnace hardware.
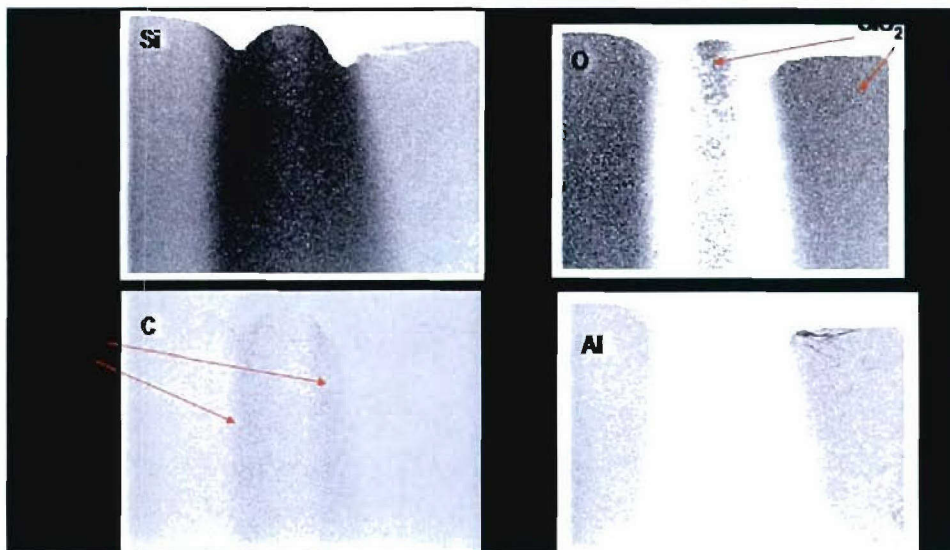


*Figure 28: EDX spectra of area shown in Fig. 25 (dark indicating high intensity signal).*

Independent measurements of recession depths and oxide thickness were obtained using an optical interference microscope. Three sets of fringes are visible in the white light interference micrograph shown in Fig. 27c: one set is from interference between reflections from the reference mirror and the top surface (oxide) of the test specimen; a second set from interference between the reference mirror and the $SiO_2$-SiC interface; and the third set from interference between the top of the oxide layer and the oxide-SiC interface. For a flat surface (i.e., before exposure to the water vapor jet), the first two sets of fringes would be straight and horizontal in Fig. 27c. The downward displacement of these fringes in Fig. 27c is proportional to the recession depth of the surface, while the separation of the two sets of fringes is proportional to the thickness of the oxide layer. The near-vertical fringes from interference between the top and bottom of the oxide layer also give a measure of the layer thickness, which increases from zero in the groove on the left to ~ 3 $\mu$m at the right side of the micrograph.

Higher magnification views of the specimen in Fig. 27 are shown in Fig. 29. Differences in the surface texture are evident in various regions: the region outside the vapor jet, which is covered with a layer of glassy $SiO_2$, is relatively smooth, whereas the region of bare SiC in the grooves is much rougher and pitted, consistent with an active oxidation process. In the central region of the vapor jet a mixture of these is seen: circular regions of bare SiC surrounded by a smoother thin film of glassy $SiO_2$. The presence of the circular regions of bare SiC suggest that breakup of the

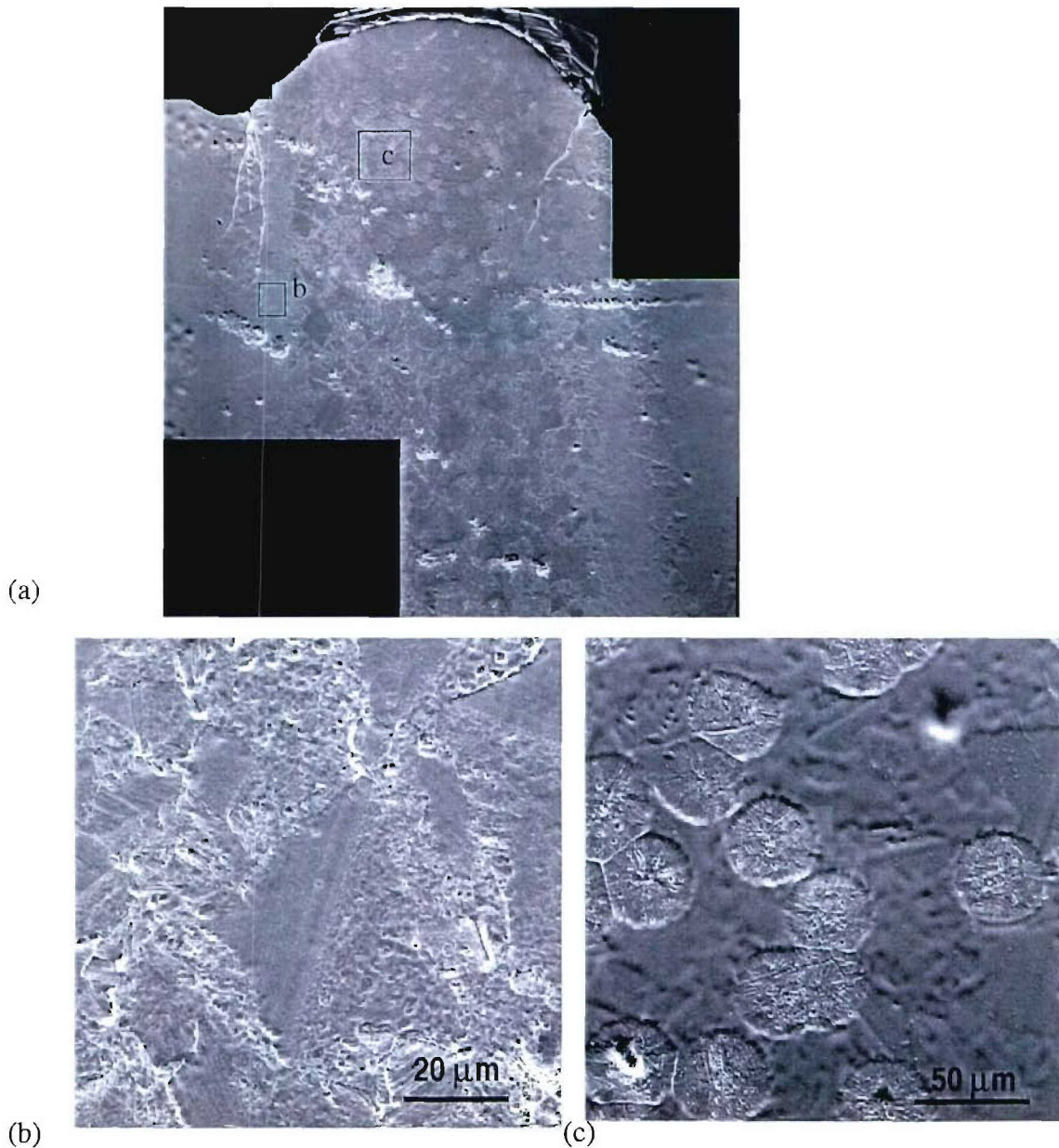oxide film may initiate with formation of gas bubbles at the interface between the SiC and the glass film.



(a)

(b)

(c)

*Figure 29: (a) Higher magnification view from area shown in Fig. 25. (b)Region indicated in (a) from groove at edge of vapor jet. (c) Region indicated in (a) from center of vapor jet.*

Erosion patterns similar to Fig. 27 were observed under several conditions of jet velocity and temperature, although the relative depths of the central region and the edge grooves varied. In some cases the side grooves were not evident. Examples of profilometry measurements over the entire surface are given in Fig. 30.
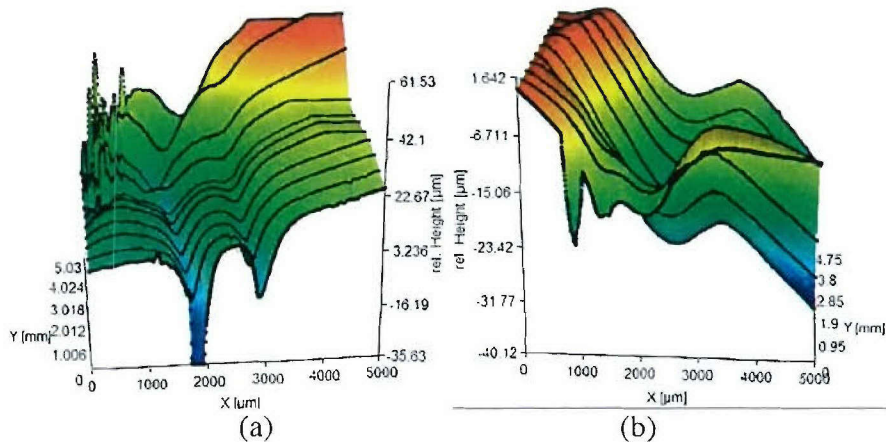
(a)          (b)

*Figure 30: 3D profilometer measurements of specimens subjected to 20 hrs at 1160°C / 1.87 ml/min (a) and 1350°C / 1.87 ml/min (b).*

**Flat test specimen configuration**

After exposure, uncoated and coated substrates showed a ring-like pattern with regions of different contrast (Figure 31). The different regions were characterized by scanning electron microscopy and showed various corrosion patterns of the SiC (Figure 32), corresponding to different flow and concentration conditions above the substrate. Further analysis by polishing and optical microscopy revealed that the ring pattern also corresponded to variations in erosion rates and silica layer thickness. As shown in the sketch in Figure 33, the substrates were eroded to a depth of several microns. This depth corresponds to an erosion rate of ~0.1 μm/hr. This relatively low erosion rate was explained by the lower temperature of the vapor at the exhaust. Calibration of the vapor temperature showed that the temperature is of the order of ~300°C with a velocity of ~300m/s. This result suggested that the steam velocity is a predominant factor in the erosion of SiC.



(a)          (b)

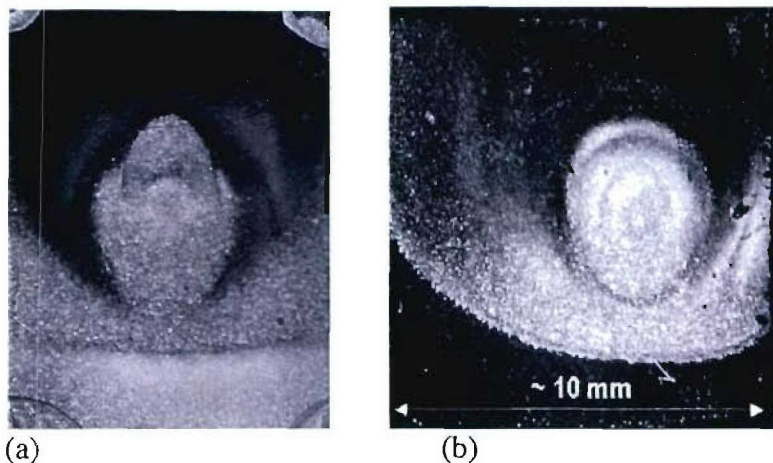*Figure 31: (a) SiC substrate and (b) La$_2$Si$_2$O$_7$ coated substrate after exposure to water impinging jet at 1400C for 16 hours*
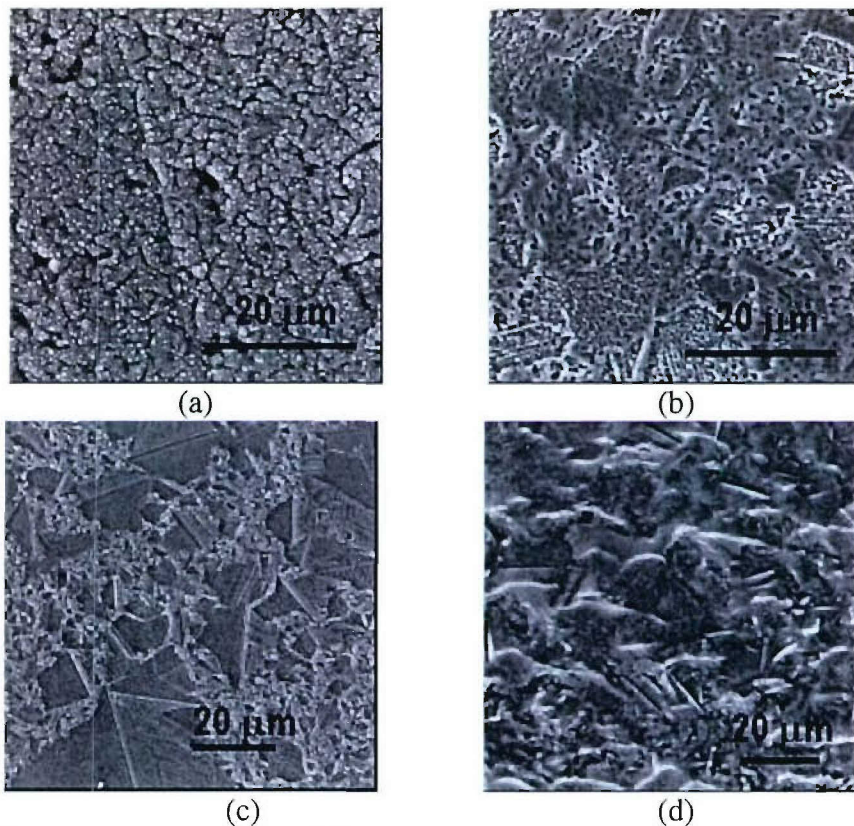
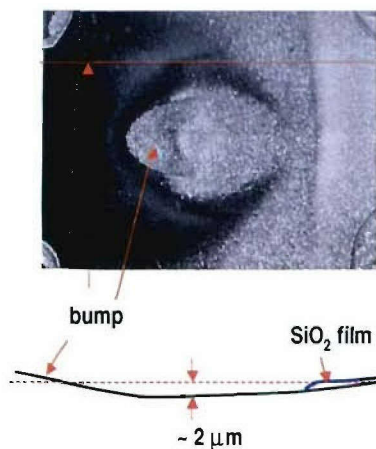Figure 32 : Microstructures at different locations on SiC samples exposed to water jet.



Figure 33:Profile of SiC substrate after test showing corrosion crater and mounds.

Exposure of a sample coated with a rare-earth silicate layer showed that the presence of the silicate coating did not modify greatly the corrosion behavior. Regions of the coating not exposed to the impinging jet were porous; some regions exhibited grain growth; and corrosion of the underlying substrate was evident in places where a coating free zone was created (Figure 34). Further experiments are required to determine the mechanisms of degradation.
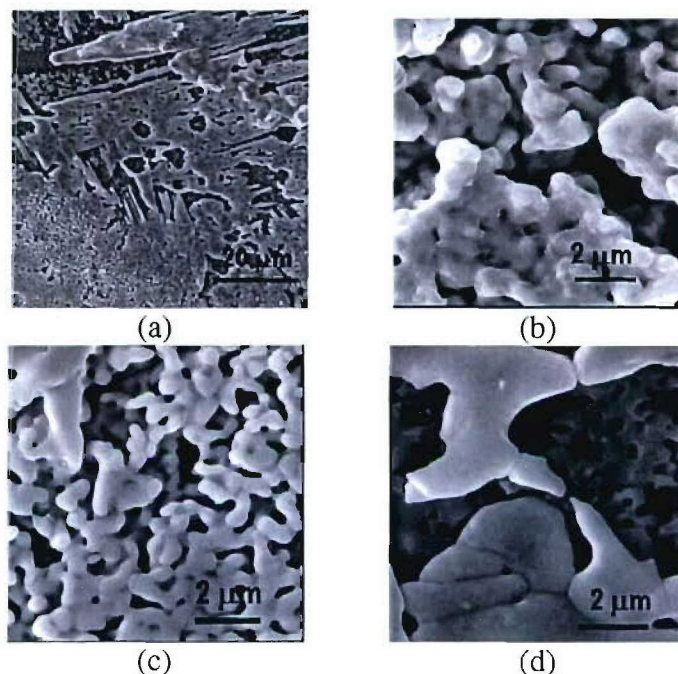
*Figure 34: (a) Region near the edge of the coating, (b) coating at the edge of the substrate, (c) and (d) details in region (a).*

## 10.5 Discussion

### Flow conditions in water vapor jet

The flow of fluid in a capillary is characterized by the Reynolds number:[21]

$$\mathrm{Re} = \frac{\rho\, d\, v_o}{\mu} \tag{4}$$

where $v_o$, $\rho$, and $\mu$ are the velocity, density, and viscosity of the fluid, and d is the capillary diameter. The flow is laminar for low values of Re, with the onset of turbulence occurring at Re = 2300 and fully developed turbulent flow at Re > 10,000. For the conditions described above we have Re < 1000. Therefore the flow at the exit of the capillary is laminar.

As the water vapor jet exits the capillary, shear forces from interaction with the surrounding slowly flowing argon gas (velocity < 0.01 m/s) generate turbulence around the boundary of the jet as depicted in Fig. 35, while the central region remains laminar. The intersection of this free-stream turbulence with surface of the test specimen in Fig. 27 corresponds with the location of the eroded grooves. This is consistent with the expectation that mass transfer would be more rapid through the boundary layer in a region of turbulent flow than in the laminar flow region in the central area of the jet.
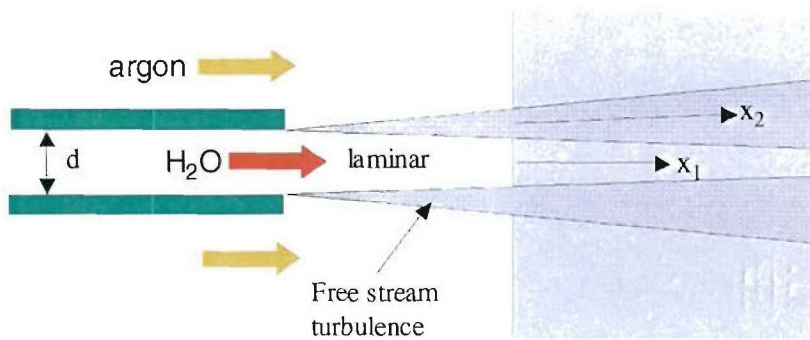
*Fig. 35. Schematic showing flow of water vapor jet over wedge-shaped test specimen. (flow rate of surrounding argon gas is low, ~ 0.01 m/s, compared with ~ 100 m/s for water jet)*

The velocity of the jet decreases with distance from the exit of the capillary.[22] However this decrease is less than ~5% within a distance of 5 times the capillary diameter. With the test specimen placed ~1mm from the capillary, this leaves a distance of several mm along the specimen surface where the velocity is almost constant.

### Influence of water vapor jet temperature on volatilization of silica

It is worth noting that, in the case of $SiO_2$ volatilization via reaction (3), the rate is relatively insensitive to temperature over the range of interest (Fig. 5), despite an exponential functional dependence (in the term $C_1$ of Eq. 1).The larger effect of temperature is likely to be in transitioning to regimes where different volatilization reactions become dominant and in affecting possible mechanisms of direct water vapor attack on the substrate under flow conditions (velocity and turbulence) for which a continuous oxide layer is unable to form.
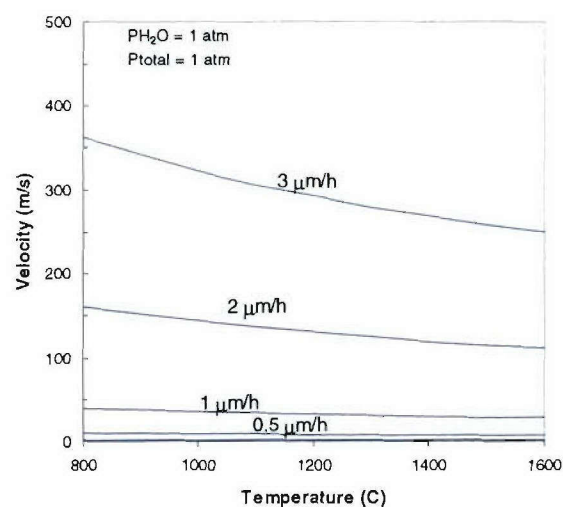


*Fig. 36. Map showing dependence of erosion rate on flow velocity and temperature for SiC with a continuous oxide surface layer (laminar flow over flat plate, thermodynamic data for Si(OH)$_4$ volatilization from Opila[8])*

## Comparison of water jet with hydrocarbon combustion

Although the partial pressure of water vapor in the 100% steam jet is the same as in an industrial turbine operating at 10 atm total pressure with 10% water vapor (typical for hydrocarbon combustion), the erosion conditions at given gas velocity depend also on the total pressure, at least within the regime where the erosion is controlled by transport of the reaction product through a laminar boundary layer (Eqs. 1 to 3). This dependence on total pressure enters via its influence on the diffusion coefficient for the reaction product through the boundary layer as well as the Reynolds number.

The dependence of the erosion conditions for $SiO_2/SiC$, on velocity, partial pressure of $H_2O$ and total pressure is shown in Fig. 6 (Eqs 1 to 3) for the laminar flow, transport-limited regime. At given velocity, the 100% steam jet gives erosion rates higher by a factor of 3 than hydrocarbon combustion at 10 atm total pressure, along with limiting oxide layer thickness smaller by a factor of 3 and time to reach steady state shorter by a factor of 10. The conditions of various test facilities and engines are shown for comparison. According to this analysis the water vapor jet can be more severe than the gas turbine engine but is less severe than a rocket engine.
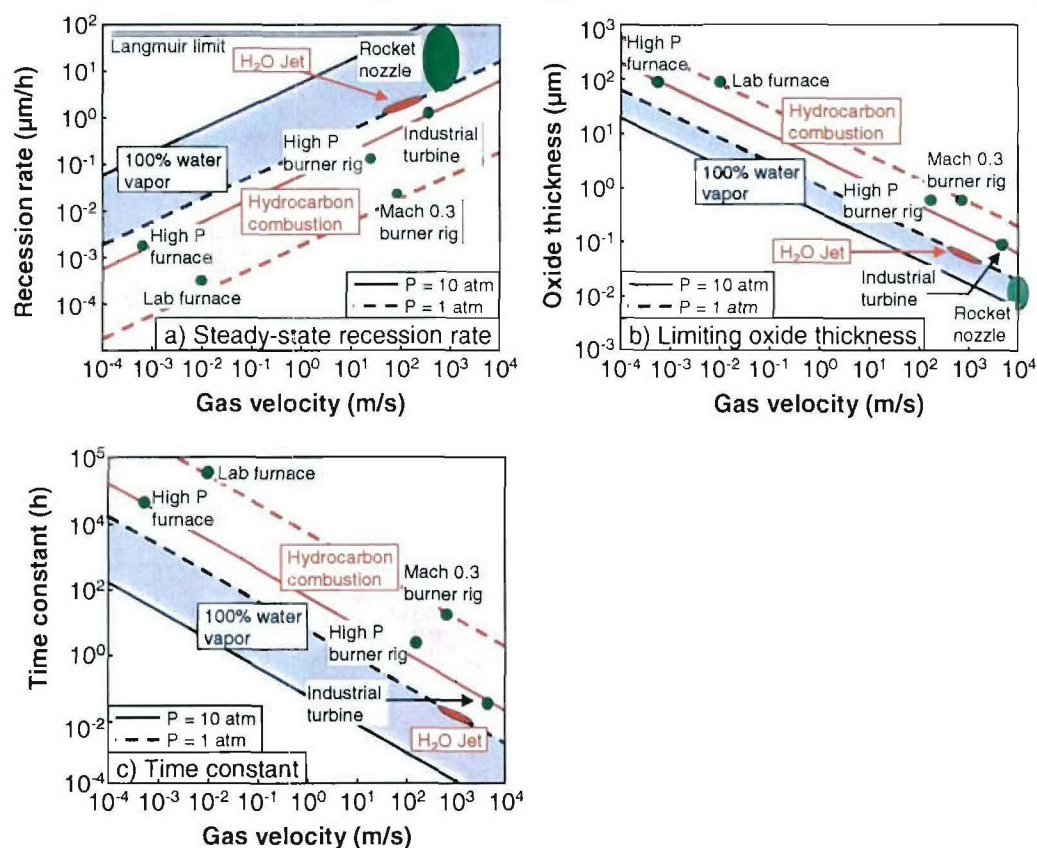


Fig. 37. Plots from Eqs. (1) to (3) comparing erosion of SiC in flowing water vapor and in hydrocarbon combustion (10% water vapor), assuming laminar flow over a flat plate and volatilization of $Si(OH)_4$: (a) steady-state recession rate, (b) limiting oxide thickness, and (c) time taken to reach steady state. Conditions corresponding to several test facilities, including our high speed water vapor jet, are indicated and compared with typical conditions for industrial turbine engines and rocket nozzles.

Under turbulent flow conditions, the mass transport rates for given velocity are higher than for laminar flow. An upper limit to this regime is given by the Langmuir equation for free evaporation into a vacuum, for which the flux of the volatile species is dependent on temperature as well as the equilibrium vapor pressure and molecular weight of the volatile species, but independent of flow velocity. This limit for $Si(OH)_4$ volatilization[2] is indicated in Fig. 35a.

**Quantitative analysis for the high velocity water vapor test**

Along the line $x_1$ in Fig. 35, where the flow is laminar, the recession rate in the transport-limited regime can be calculated following the analysis of Opila,[20] which begins with a dimensionless correlation function for the Sherwood number, Sh, in terms of the Reynolds number, Re, and Schmidt number, Sc:

$$Sh = \frac{k_1 L}{D\rho_v} = 0.664 \, Re^{1/2} \, Sc^{1/3} \tag{5}$$

$$k_1 = 0.664 \left(\frac{Lv\rho}{\eta}\right)^{1/2} \left(\frac{\eta}{\rho D}\right)^{1/3} \frac{D\rho_v}{L} \tag{6}$$

where $k_1$ is the mass flux, v is the gas velocity, $\rho_v$ the equilibrium concentration of $Si(OH)_4$, $\rho$ the concentration of boundary layer gas, D the diffusion coefficient, and $\eta$ the gas viscosity. For the case of Si-containing materials with reaction (3) to give $Si(OH)_4$, Eq. 5 reduces to Eq. 1.

In the turbulent boundary region (line $x_2$ in Fig. 35), where the erosion rate is considerably higher, a similar dimensionless correlation for the Sherwood number could be used for quantitative analysis.

## 10.6  Summary and outlook

The method demonstrated here provides a means for efficient laboratory scale studies of corrosion of materials and coatings by water vapor, under conditions that are representative of the gas velocity, partial pressure, and temperatures of full-scale gas turbine engines. The configuration with a sharp wedge-shaped test specimen appears to be most suitable for quantitative analysis of mass transport through a well controlled boundary layer. Along the centerline of the vapor jet, the conditions are laminar and analytical solutions are available. Around the periphery of the jet, where the free stream turbulence creates much higher mass transfer conditions (and hence erosion rates), numerical CFD solutions will allow quantitative analysis. The presence of two regions with well defined sets of conditions in the one test is a useful feature.

This test setup should prove useful for obtaining fundamental data on volatilization of compounds under consideration for new protective coatings. Especially important is the ability to compare the responses of single-phase compounds and multiphase coatings to allow separation of intrinsic behavior of the constituents and the effects of microstructure in multiphase coatings. With the very large range of conditions (velocity and temperature) readily available, systematic studies of transitions between regimes of different controlling mechanisms (e.g., protective oxide scale to active oxidation) will be possible.

# 11 Conclusions

The electron beam ablation technique was used to deposit coatings of lanthanum phosphate and lanthanum silicate. The technique was investigated to improve the deposition of coating compounds that are known to be difficult to deposit by conventional electron-beam evaporation. We have demonstrated that crystalline compounds form on substrates heated at high temperatures using electron-beam ablation and heated stationary or rotating heated substrates. However, the phases formed had a composition different from those of the target material. . We have found that the stoichiometry varies as a function of distance from the center of the plume as species of lesser atomic mass diffuse faster than heavier species. The control of the stoichiometry was eventually achieved using an off-stoichiometry target to compensate for the loss. Although coatings of $LaPO_4$ monazite have been successfully deposited, the control of the stoichiometry is difficult over large areas.

We have developed a technique to characterize materials in water-rich environments similar to those found in combustion engines and rockets. Water vapor corrosion rates of ~1 $\mu$m/hour have been demonstrated for a range of temperature and water-vapor velocity conditions. This new technique opens the way for advanced characterization of high temperature materials and coatings that are candidates for use in hot sections of heat engines and rockets.

# 12 References

1.  O. Sudre, J. Cheung, D. Marshall, Peter Morgan and C. Levi, " Thermal Insulation Coatings of LaPO4," Cer. Eng. Sci. Proc., vol.22 [4] pp.367-374 (2001).
2.  E.J. Opila and R.E.J. Hann, "Paralinear Oxidation of CVD SiC in Water Vapor," *J. Am. Ceram. Soc.,* **80**[1] 197-205 (1997).
3.  Lee KN, Fox DS, Bansal NP ,"Rare earth silicate environmental barrier coatings for SiC/SiC composites and Si3N4 ceramics," J. Eur. Cer.Soc. 25 (10): 1705-1715 2005.
4.  R. Stark, J. Christiansen, K. Frank, "Pseudospark Produced Pulsed Electron Beam for Material Processing" IEEE Transactions on Plasma Science, **23**[3] 258-64 (1995)
5.  M. Hobel, J. Geerk, G. Linker and C. Schultheiss, "Deposition of superconducting YBaCuO thin films by pseudospark ablation" Appl. Phys. Lett. **56**[10] 973-5 (1990).
6.  G. Muller, M. Konijnenberg, G. Krafft, C. Schultheiss, "Thin Film Deposition by means of pulsed electron beam ablation" in Science and Technology of thin films, World Scientific 1995.
7.  V.I. Dediu, Q.D. Jiang, F.C. Matacotta, P. Scardi, M. Lazzarino, G. Nieva, L. Civale, "Deposition of MBa2Cu3O7-x thin films by channel-spark method," Supercond. Sci. and Tech., **8**[3] 160-164 (1995)
8.  S.D. Kovaleski, R.M. Gilgenbach, L.K. Ang, Y.Y. Lau, J.S. Lash, "Electron beam ablation versus laser ablation: plasma plume diagnostic studies", Applied Surf. Sci. **127-129** 947-952 (1998).
9.  E.M. Levin, C.R. Robins and H.F. McMurdie, Phase Diagrams for Ceramist, 1969 Supplement (The American Ceramic Society, Westerville OH, Fig. 2372.
10.  A.S. Risbud, K.B. Helean, M.C. Wilding, P.Lu and A. Navrotsky, "Enthalpies of Formation of Lanthanide Oxyapatite Phases," J. Mater. Res., Vol. 16, No. 10, Oct. 2001.
11.  Lee, K. N., Miller, R. A. and Jacobson, N. S., New generation of plasma-sprayed mullite coatings on silicon-carbide. *J. Am. Ceram. Soc.*, 1995, **78**(3), 705–710.
12.  Lee, K. N., Fox, D. S., Eldridge, J. I., Zhu, D., Robinson, R. C., Bansal, N. P. *et al.*, Upper temperature limit of environmental barrier coatings based on mullite and BSAS. *J. Am. Ceram. Soc.*, 2003, **86**(8),1299–1306.
13.  Price, J. R., van Roode, M. and Stala, C., Ceramic oxide-coated silicon carbide for high temperature corrosive environments. *Key Eng. Mater.*, 1992, **72–74**, 71–84.
14.  Lee, K. N., Current status of environmental barrier coatings for Sibased ceramics. *Surf. Coat. Technol.*, 2000, **1–7**, 133–134.
15.  Lee, K. N., Fox, D. S., Eldridge, J. I., Zhu, D., Robinson, R. C., Bansal, N. P. *et al.*, Upper temperature limit of environmental barrier coatings based on mullite and BSAS. *J. Am. Ceram. Soc.*, 2003, **86**(8), 1299–1306.
16.  Eaton, H. E., Linsey, G. D., Sun, E. Y., More, K. L., Kimmel, J. B., Price, J. R. *et al.*, EBC protection of SiC/SiC composites in the gas turbine combustion environment— continuing evaluation and refurbishment considerations. ASME paper 2001-GT- 0513 ASME TURBOEXPO 2001. June 4–7, 2001. New Orleans, Louisiana.
17.  More, K. L., Tortorelli, P. F., Walker, L. R., Kimmel, J. B., Miriyala, N., Price, J. R. *et al.*, Evaluating environmental barrier coatings on ceramic matrix composites after engine and laboratory exposures. ASME paper 2002-GT-30630. In *Proceedingsof ASME Turbo Expo 2002*, June 3–6, 2002. Amsterdam, The Netherlands.

18. Kang N. Lee., Dennis S. Fox, Narottam P. Bansal, "Rare earth silicate environmental barrier coatings for SiC/SiC composites and Si3N4 ceramics," Journal of the European Ceramic Society **25,** 1705–1715 (2005)
19. M-K Ferber and H-T Lin, "Environmental Characterization of monolithic Ceramics for gas Turbine Applications," Key Engineering Materials Vol. 287 (2005), pp. 368-380
20. E. J. Opila, "Oxidation and Volatilization of Silica Formers in Water Vapor," *J. Am. Ceram. Soc.,* **86** [8] 1238–48 (2003)
21. F. P. Incropera and D. P. Dewitt, "Introduction to Heat and Mass Transfer," Wiley
22. H. Martin, "Heat and Mass Transfer Between Impinging Gas Jets and Solid Surfaces," Advances in Heat Transfer, 13  1-60 (1977)